DEVELOPMENT OF A LASER SCANNING MEASUREMENT SYSTEM FOR BATTERY CELL CHARACTERIZATION

by

Zachary Simunovic

Submitted in partial fulfilment of the requirements
for the degree of Master of Applied Science

at

Dalhousie University
Halifax, Nova Scotia
August 2023

Dalhousie University is located in Mi'kma'ki, the ancestral and unceded territory of the Mi'kmaq. We are all Treaty people.

Table of Contents

List of Tables

List of Figures

Abstract

A precise understanding of the physical properties of lithium-ion cells including cell thickness distribution during cycling and its connection with lifetime is important for cell improvement. A laser scanning instrument has been developed to perform contact-free thickness measurements in operando for small 250 mAh lithium-ion pouch cells and a large 60 Ah automotive format pouch cell. $LiNi_{0.83}Mn_{0.07}Co_{0.10}O_2$/silicon-graphite cells with 20 and 10 wt% micron-sized silicon particles, a $LiNi_{0.8}Mn_{0.1}Co_{0.1}O_2$/natural graphite cell, and a medium-Ni/graphite automotive cell were either cycled in the laser scanning setup with continuous operando thickness mapping or aged at elevated temperature on separate battery cyclers with intermittent operando thickness mapping using the new laser scanning instrument. During the operando cycles, the cell thickness was measured periodically every 1 hour and a graphical quantification method was developed to determine reversible and irreversible swelling of the silicon-containing and silicon-free cells. Using the high-resolution laser scanning technique, irreversible cell swelling could be correlated with capacity loss, especially in cells with high silicon content. Graphite-based cells with mature interface like the large automotive pouch cell showed a fully reversible swelling profile indicative of a long-lived cell.

List of Abbreviations and Symbols Used

AG	Artificial graphite
BOD	Bottom of discharge
CE	Coulombic efficiency
CT	Computed tomography
DMC	Dimethyl carbonate
DTD	1,3,2-Dioxathiolane-2,2-dioxide
e	Elementary charge
EC	Ethylene carbonate
EMC	Ethyl methyl carbonate
F	Faraday's constant
FEC	Fluoroethylene carbonate
LCO	Lithium cobalt oxide ($LiCoO_2$)
LEDC	Lithium ethylene dicarbonate
LFP	Lithium iron phosphate
LIB	Lithium-ion battery
Li-ion	Lithium-ion
LMFP	Lithium manganese iron phosphate
LMO	Lithium manganese oxide
NG	Natural graphite
NMC	Lithium nickel manganese cobalt oxide ($LiNi_{1-x-y}Mn_xCo_yO_2$)
SEI	Solid electrolyte interphase
Si-C	Silicon carbon composite

Si-G	Silicon graphite
SiO	Silicon oxide
SOC	State of charge
TOC	Top of charge
μ_{neg}	Negative electrode chemical potential
μ_{pos}	Positive electrode chemical potential
VC	Vinylene carbonate
V_{OC}	Open circuit voltage
Δz_{charge}	Change in thickness during charge
Δz_{irrev}	Irreversible thickness change

Acknowledgments

I greatly appreciate all the people who had taken the time to provide support and guidance to me over the course of my master of applied science.

Primarily, I would like to thank my research supervisor Michael Metzger for all of his outstanding teaching and patience, and my administrative supervisor Jeff Dahn for the excellent oversight he provided. I am also very grateful for all of the mentors and colleagues I made during my time in the Dahn-Metzger-Yang group. This was an amazing lab group to be a part of, I learned a great deal and it was inspiring to be around so many passionate and talented engineers and scientists.

I would also like to thank the mechanical engineering department for their administrative support, and my committee members Lukas Swan, and Chongyin Yang for their helpful feedback.

I would also like to acknowledge Chris McMonigle and Michael Fisher from LMI Technologies Inc. for providing the Gocator 2520 laser sensors for my thesis project, and their constructive discussions. I also acknowledge Simon Trussler and Mike Johnson for their assistance in constructing the laser scanning set up.

Chapter 1: Introduction

1.1 Motivation

Lithium ion batteries (LIBs) have enabled the widespread use of consumer electronics and are in the process of powering the transition to electric vehicles, though LIBs are facing several key challenges to meet the requirements of the automotive sector. The more stringent technical requirements for automotive use are assessed in terms of energy density, lifetime, cost, safety, and fast charge capability.[1] Graphite as a negative electrode material for LIBs provides low volume expansion during lithiation, good cycle life, and high coulombic efficiency (CE); further improvements of the negative electrode can be made with alloy-based electrode materials.[2] Silicon is of high interest for use as a negative electrode in LIBs as it has a higher specific and volumetric capacity (3579 mAh/g and 2194 Ah/L) than graphite (372 mAh/g and 719 Ah/L), which leads to improved energy density.[2] Though, this large capacity increase has a downside, as lithium-ion (Li-ion) cells with high silicon content in the negative electrode have poor cycle life due to a large volume expansion of 280% for silicon particles during lithiation and delithation.[2] This large volume expansion can cause current collector distortion at the cell level, it can damage the solid-electrolyte interphase (SEI) at the particle level, and it can cause particles to fracture at the sub-particle level; all of which are factors that lead to capacity fade.[2]

There are many characterization methods in the literature that focus on electrode or cell thickness measurements as a tool for learning about the reversibility of electrochemical reactions at the electrode/electrolyte interfaces and cell failure mechanisms. Synchrotron computed tomography (CT) scans have been able to detect micro-cracking of positive electrode particles causing swelling which leads to an increase in positive electrode layer thickness, jelly roll distortion, delamination from the aluminum current collector, and depletion of excess electrolyte.[3] Though this method has a very long scan time, limited availability and an extremely high cost limiting widespread application. There have been electrochemical dilatometry techniques used to measure volume expansion including a dilation cell, which can

detect electrode expansion for homogenous and inhomogeneous pressure distributions.[4] These techniques are useful since volume changes of LIBs during cycling and aging as well as increased pressure in volumetrically constrained cells can typically not be tolerated in commercial devices with optimized packing. There are also in-situ pressure measurement instruments, which are used to measure the electrode volume expansion on volumetrically constrained pouch cells to better understand swelling.[5] Though, dilatometry measures electrode expansion, and in-situ pressure measurement techniques measure the average pressure exerted by the entire cell surface, neither of these techniques can determine *where* swelling takes place. It is important to determine where swelling occurs because a cell with uneven swelling distribution is more prone to having a reduced cycle life and safety issues. Parts of a cell that have more pressure build up will have more thickness change leading to more irreversibility, and there is higher chance of lithium plating at the edges of a cell.[6,7] There is need to develop a rapid characterization method at relatively low cost that can quantify volume expansion and the location of cell swelling with high-resolution, while also being able to investigate the electrochemical performance.

1.2 Scope of this Work

In this work, I present a laser scanning measurement technique (see Fig. 1.1 for a general system layout) to study small Li-ion pouch cells and large format automotive pouch cells. There are existing laser scanning measurement systems that have been used to measure electrode stack thickness growth in LIBs. In comparison to the laser scanner method developed in this work, a multi-directional laser scanner was built to measure thickness change at various temperatures, and to detect lithium plating.[8,9] Another laser scanning system was developed to measure how cell swelling varies based on different charge and discharge rates, and it was used to detect cell inhomogeneties.[10] These techniques also use built in tools to calculate the local thickness change for approximately 100 sections of the cell surface; whereas the method in this work uses a data analysis technique to create accurate thickness mapping over an entire cell surface and calculate an average thickness change over every data point (Section 3.2 explains the

specifics) on the cell surface. Furthermore, the other systems have neither been used on silicon-containing cells that are notorious for swelling, nor have they been used on large automotive pouch cells for which swelling can be a safety hazard as it can lead to tearing of current collector tabs and other safety relevant failure modes.[11]

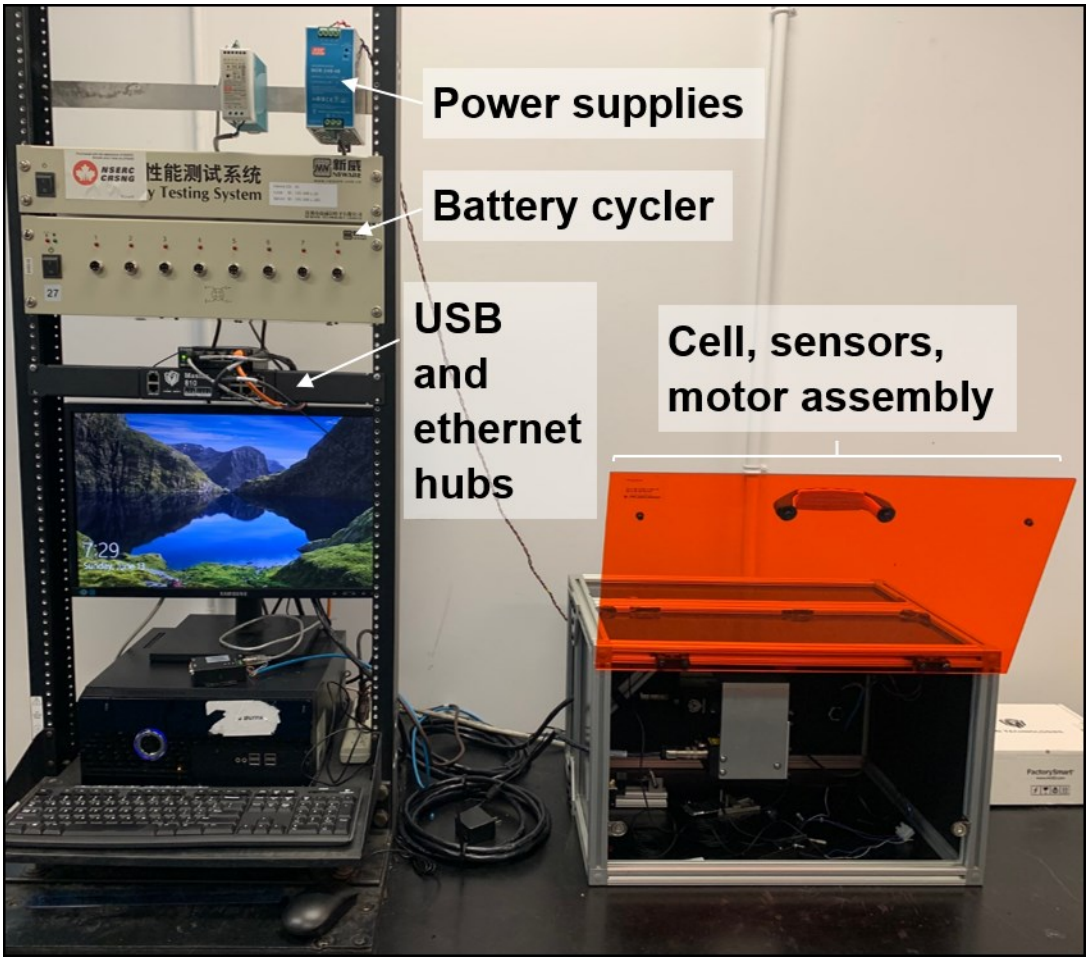

Figure 1.1: Picture of laser scanning setup connected to a Neware battery cycler.

Using the new method, rapid and contact free operando measurements with a lateral resolution of 15 µm and a high thickness resolution of 0.57 µm were performed on Li-ion pouch cells with different silicon content in the negative electrode and a large automotive cell with a medium-nickel/graphite cell chemistry. The laser scanning technique in operando can show cell swelling with high accuracy and provide insight on electrochemical performance including a

relationship between reversibility of thickness growth, capacity fade and CE. Lastly, this new technique is capable of measuring cell swelling safely at any point of cycle life.

Chapter 2 provides an introduction on LIBs; a description on the main components of Li-ion cells including the electrolyte and the positive and negative electrode active materials, as well as a discussion on battery aging. Chapter 3 presents the experimental work performed in this thesis like pouch cell preparation, cycling, and more specifically the details on the method development of the new laser scanner technique. Chapters 4 and 5 describe the results of this thesis for the volume expansion of silicon containing cells and large automotive pouch cells, respectively. Chapter 6 presents a discussion on conclusions and future work for this thesis.

The work presented in this thesis, specifically the development of the laser scanner, and the results shown in Chapters 4 and 5, are part of a manuscript in preparation: Zachary Simunovic, Reid Dressler, Ethan D. Alter, Simon Trussler, Jessie Harlow, Mike Johnson, Chris McMonigle, Michael Fisher, and Michael Metzger, “Laser Scanning Method for High-resolution Thickness Mapping of Li-ion Pouch Cells” (2023). For the manuscript in preparation, I was responsible for the research development, design, experimentation, analysis, and writing.

Chapter 2: Lithium-Ion Batteries

An LIB is a rechargeable battery that uses an electrochemical process of converting stored chemical energy into useful electrical energy during discharge, and then the reverse reaction occurs during charge. An LIB is built by connecting Li-ion cells in series to increase voltage, or in parallel to increase the current, or in combination to deliver the desired battery characteristics.

2.1 Lithium-Ion Cells

Figure 2.1 shows the primary functional components of a typical Li-ion cell which are the negative electrode (anode), the positive electrode (cathode), and the electrolyte. The most common negative electrode is graphite coated onto a copper current collector. Positive electrode materials are usually lithium transition metal oxides such as lithium cobalt oxide ($LiCoO_2$ or LCO), that are coated onto an aluminum current collector. The electrolyte usually contains a lithium salt (most commonly lithium hexafluorophosphate or $LiPF_6$) that is generally dissolved in a solvent made from a mixture of organic carbonates. The electrodes are the materials where the chemical energy is stored, and they have layered structures allowing for lithium to intercalate. During discharge, the lithium ions move through the electrolyte and intercalate into the positive electrode, and during charge, the lithium ions move back into the negative electrode. The electrolyte serves as the transport medium for lithium ions allowing for the storage and movement of electrical energy between each electrode. The two electrodes are also separated by a porous film called a separator that is usually made of a polyolefin material. These commonly used separators are good electric insulators forcing electrons to flow through a closed external circuit in order to do useful work and prevent short circuits.[12]

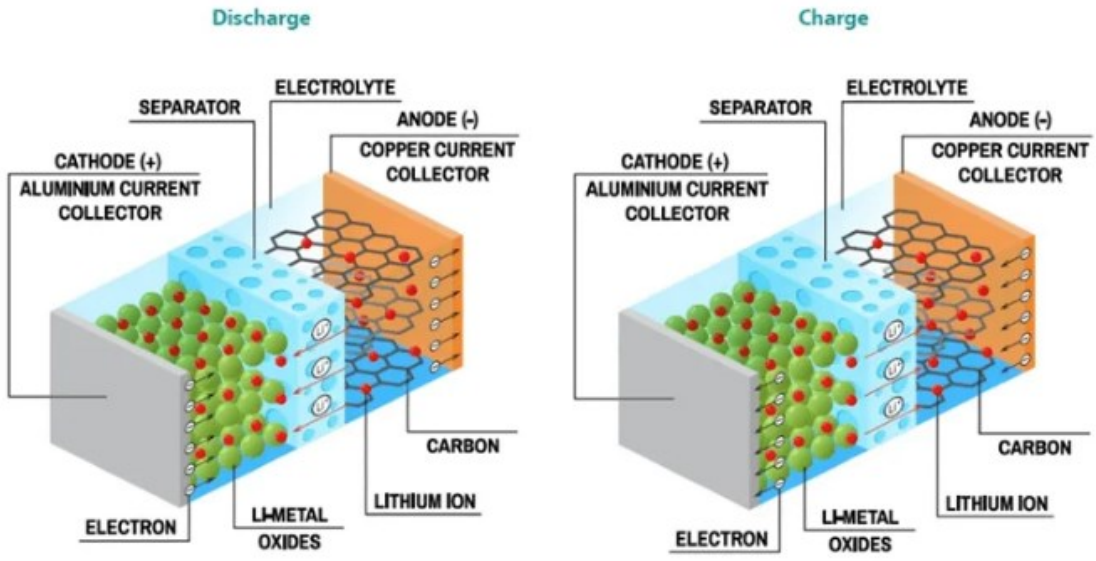

Figure 2.1: Schematic of a Li-ion cell during discharge (left) and charge (right). The image is obtained from Ref. 13.

Redox reactions occur during discharge/charge cycles, where lithium ions and electrons are moved between each electrode. During discharge, the transition metal in the lithium transition metal oxide positive electrode is reduced (e.g., Co in $LiCoO_2$), and during charge it is oxidized as per Equation 2.1. The reverse happens for the negative electrode; during discharge carbon (C) in the graphite negative electrode is oxidized, and during charge it is reduced which is represented by Equation 2.2. The overall cell reaction is given by Equation 2.3 which describes the reversible movement of lithium ions from one electrode to another.

$$\text{Positive electrode: } Li_{1-x}CoO_2 \Leftrightarrow LiCoO_2 - xe^- - xLi^+ \quad (2.1)$$

$$\text{Negative electrode: } yLi_{x/y}C_6 \Leftrightarrow yC_6 + xe^- + xLi^+ \quad (2.2)$$

$$\text{Full cell: } Li_{1-x}CoO_2 + yLi_{x/y}C_6 \Leftrightarrow LiCoO_2 + yC_6 \quad (2.3)$$

There is a difference in chemical potential between the positive and negative electrodes which creates the driving force (also electromotive force) to move the electrons and lithium ions back and forth between the electrodes. This is known as the open-circuit voltage (V_{OC}), and it is determined by the difference of chemical

potentials (μ) of the active materials in the electrodes. V_{OC} is given by Equation 2.4 where e is the elementary charge.[14]

$$V_{OC} = (\mu_{neg} - \mu_{pos})/e \quad (2.4)$$

Li-ion cells are assessed in terms of many parameters to ensure commercial success which primarily include high power density (W/kg or W/L), high energy density (Wh/Kg or Wh/L), cycle life, safety, and low cost. There are many researchers that work to optimize these parameters to enable the commercial success of LIB applications in the consumer electronic market, for grid storage, and for use in electric vehicles.[12]

2.2 Electrode Materials

The positive and negative electrodes in a Li-ion cell contain active materials that are critical for determining its performance characteristics. This section will discuss the active materials used in Li-ion cell electrodes; where the electrodes used in this work consist of >95% active material, and <5% binder and conductive additive combined.

2.2.1 Positive Electrode Materials

The favorable requirements of a positive electrode active material include having a readily reducible/oxidizable atom like a transition metal that can react with lithium with a high free energy of reaction to obtain a high voltage and thus a high energy density cell. The properties of the active material that can impact battery performance include the shape, size, and distribution of particles. Li-ion cells most commonly use a lithiated transition metal oxide as the active material such as LCO. LCO is very common; primarily due to providing good cycle life and higher energy density. There are also many researchers that look at iron to be used in cathode materials which includes lithium iron phosphate ($LiFePO_4$ or LFP). LFP has the potential to make a large impact in Li-ion cells due to its low cost and environmentally friendly characteristics, though its specific capacity is lower in comparison to nickel and cobalt based materials. Lithium manganese iron

phosphate ($LiMnFePO_4$ or LMFP) is another type of cathode material obtained by adding manganese to LFP, which raises the voltage and provides an increase in energy density. Another cathode material that is used is lithium manganese oxide ($LiMn_2O_4$ or LMO). LMO is promising for use in energy storage applications due to its high power, safety, and low cost. Though eventually, the introduction of cobalt and manganese into nickel oxide structures such as lithium nickel manganese cobalt oxide ($LiNi_{1-x-y}Mn_xCo_yO_2$ or NMC) lead to a more stable structure while improving cycling performance at even higher temperatures, having larger battery capacity, and reducing cost due to minimizing the use of cobalt. These are all factors that make nickel-rich materials a promising cathode material for energy storage and electric vehicle applications. The NMC stoichiometries used in this thesis are NMC532 ($LiNi_{0.5}Co_{0.3}Mn_{0.2}O_2$), and NMC811 ($LiNi_{0.8}Co_{0.1}Mn_{0.1}O_2$).[12]

2.2.2 Negative Electrode Materials

The favorable requirements for a negative electrode active material include having minimal volume expansion during charge and discharge. The most commonly used negative electrode material for Li-ion cells is graphite; an intercalation compound that stores lithium between graphene sheets, and can insert lithium up to a stoichiometry of LiC_6. There are two types of graphite that are generally used in Li-ion cells. They are natural graphite (NG), and artificial graphite (AG) which are both used in this thesis. Natural graphite is a naturally occurring material that exists in nature, and artificial graphite is synthesized by pyrolyzing a carbon precursor at very high temperatures of around 3,000°C. Natural graphite is used for Li-ion cell anode materials due to its high reversible capacity and low cost, whereas artificial graphite has structures that can facilitate effective lithium intercalation allowing for smaller irreversible capacity that is associated with ongoing electrolyte decomposition.[12] Overall, graphite is a widely used active material for negative electrodes in Li-ion cells for its exceptional electrochemical properties. It has a very low volume expansion (10% for full (de-) lithiation), a low voltage hysteresis and irreversible capacity, it has good cycle life and rate capability, a high CE, and it is based on an abundant and inexpensive material. Though, graphite has a relatively low specific and volumetric capacity (372 mAh/g

and 719 Ah/L) compared to some other anode active materials. In particular, there is a very strong interest in the development of silicon-based anode materials due to having a very large specific and volumetric capacity (3579 mAh/g and 2194 Ah/L). However, silicon negative electrodes do not have many of the same excellent properties that graphite possesses as mentioned above. In fact, silicon anodes experience a very large volume expansion (280% for full (de-) lithiation), they have a large voltage hysteresis, and poor cycling performance.[2]

Silicon based negative electrodes do not have the same lithium intercalation process like graphite. The lithium alloys with silicon after lithium insertion causing large volume expansion. The large volume expansion, along with loss of electrical contact, and particle fracture are among many factors that cause silicon to have poor cycle life hindering the commercial adoption of silicon based anodes.[2,12] There are different approaches that researchers have used to reduce the poor electrochemical characteristics of silicon. This includes using nanosized particles to limit particle fracture, and alloying active material with inactive material such as $FeSi_2$, $CoSi_2$, or $NiSi_2$ to reduce volume expansion.[2]

Many researchers have made advances in silicon based alloy anodes with engineered structures such as silicon based alloy nanoparticles, silicon nanowire, porous silicon, and thin film silicon. Nano silicon anodes possess larger specific capacity and better capacity retention than micron silicon. They also have good strain capabilities that can reduce mechanical fracture and improve the safety of LIBs. Silicon nanowire consists of a one dimensional structure where an array of silicon alloy nanowire grows directly on the current collector. This structure can alleviate the pulverization of silicon anodes and achieve a higher capacity retention due to having a higher lithium diffusion rate. Porous silicon design can help reduce the issue of large volume expansion in silicon anodes. Porous structures can be synthesized by using porous templates, or chemical and electrochemical corrosion techniques which result in structures that can reduce stress on the electrode and improve cycling stability. Thin film silicon is another structure that addresses the issues of severe volume change, and these films can range from thickness of sub

nanometers to several microns. This thin film structure has a large surface area to volume ratio which improves the transfer of electrons and Li-ions, as well as reduce the mechanical stress induced by Li-ion insertion and extraction. Microstructure engineering techniques for silicon anodes is a viable method for reducing volume expansion of silicon based anodes, however these techniques tend to result in larger surface areas which result in more side reactions and thus higher irreversible capacity loss.[15]

There are a variety of forms that silicon is used in LIBs as a negative electrode. Silicon carbon composite (Si-C) is a compound that consists of nano-grains of silicon coated with carbon. Si-C is used in LIBs for its ability to combine the high volumetric energy of silicon with the low volume expansion of carbon. Silicon oxide (SiO) consists of a nano-structure of Si and SiO_2. Using an average voltage of silicon of 0.4 V, SiO can contribute to a stack energy density of 853 Wh/L based on a full cell model described in Ref. 2, making it a good negative electrode for high energy density cells. Though, SiO has a high irreversible capacity that needs to be resolved for SiO to be widely adapted in the use of LIBs. Natural silicon which is used in this thesis, is a compound where the silicon microstructure consists of micron sized silicon particles that are composited with graphite. Natural silicon is used in this thesis since it has a very high specific capacity and because it undergoes large volume changes which is generally undesired but suitable here for demonstrating the usefulness of the laser scanning technique.[2]

2.3 Electrolyte

The electrolyte is an important component of a Li-ion cell, and its purpose is to act as an ionic conductor for the transfer of charges, that are in the form of solvated ions, between the positive and negative electrodes during charge and discharge. The liquid electrolyte must be capable of seeping into the porous electrodes, and transfer the lithium ions efficiently at the interface between the liquid and solid phases. Desirable solvent qualities are good ionic conductivity, a high dielectric constant (to allow salts to dissolve at large concentrations), low viscosity, and stability over a wide range of operating temperatures and electrochemical

potential. The electrolyte most commonly used in Li-ion cells is $LiPF_6$ dissolved in organic carbonate solvents including ethylene carbonate (EC), ethyl methyl carbonate (EMC), and dimethyl carbonate (DMC). $LiPF_6$ has been successful and widely used due to possessing many of the desired properties including high ionic conductivity, sufficient thermal and electrochemical stability, as well as the ability to passivate the aluminum current collector.[12]

There are two electrolytes used in this study. The electrolyte for silicon-containing cells consists of EMC and fluoroethylene carbonate (FEC) in a weight ratio of 8:2, and it uses a dual lithium salt with no additives. The electrolyte for silicon-free cells consists of EC, EMC, and DMC in a weight ratio of 25:5:70, and it uses 1.5 M $LiPF_6$ as a lithium salt, and additives of 2 wt% vinylene carbonate (VC) and 1 wt% 1,3,2-Dioxathiolane-2,2-dioxide (DTD). The electrolyte components were all used as received (<20 ppm water) from Shenzhen Capchem (China) and mixed in an argon-filled glovebox.

The silicon containing cells used FEC as it has shown to prevent most of the initial reduction of EMC and lower gaseous products.[16] Electrolyte additives are generally added in small amounts that have been known to improve the performance of Li-ion cells. The electrolyte and additives used for the silicon-free cells are known to work well with the electrode chemistry they are paired with.[17]

2.4 Lithium-Ion Cell Degradation

The capacity of a Li-ion cell will decrease over cycling due to components that slowly degrade, which includes the electrodes and the electrolyte. The lithium that is used to provide energy can become consumed by degradation mechanisms, reducing the available lithium inventory and resulting in capacity loss of the Li-ion cell. The degradation mechanisms that cause battery aging can also lead to volume expansion of the Li-ion cell, and this section will discuss these mechanisms and how they can impact the lithium loss and expansion of LIBs.

2.4.1 The Solid Electrolyte Interphase (SEI)

The solid electrolyte interphase is a passivating film that is formed during the first electrochemical reaction of an electrode. During this reaction, the active lithium

reacts with electrolyte products at the negative electrode creating the film which acts as an interphase between the electrode surface and the electrolyte solution. The SEI is a good ionic conductor and electronic insulator, that is generally composed of insoluble and partially soluble reduction products of the electrolyte components. The favorable properties of a good SEI also include mechanical stability, flexibility, and adhesion to the anode which are optimized during the first charge (formation step). This formation helps prevent solvent decomposition, and is critical for enhancing cycling performance, and the SEI can be improved by use of electrolyte additives. Though, the formation of the SEI is also primarily responsible for the large irreversible capacity on the first charge due to the large consumption of lithium that is not recovered during the first discharge.[12] Figure 2.2 is a model for the SEI composition that consists of many materials including inorganic compounds like LiF, Li_2O, insoluble components like Li_2CO_3, and partially soluble semi-carbonates and polymers. The SEI continues to grow with repeated fracture and repair over cycling contributing to a loss of lithium to the SEI resulting in capacity loss, and thus battery aging.[18]

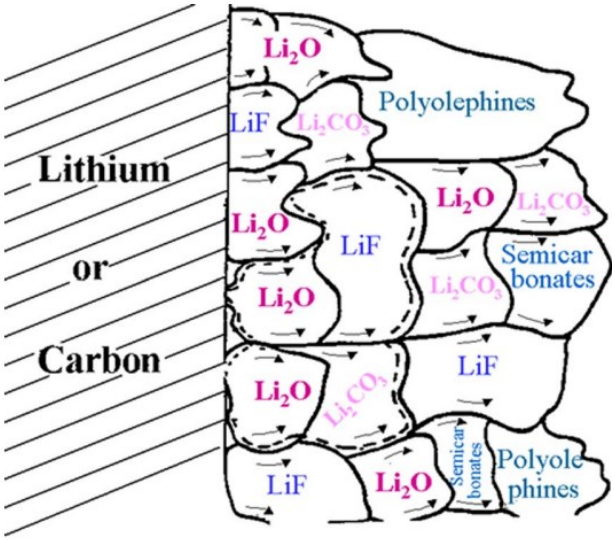

Figure 2.2: Schematic representation for a SEI. The graphic comes from Ref. 18.

2.4.2 Stack Thickness Growth

High energy density positive electrode materials that have high nickel content like NMC can experience volume expansion during repeated cycling that can produce

mechanical stress on the cathode material which is a critical Li-ion cell degradation mode. Nickel rich polycrystalline (individual grains of various size and orientation) NMC materials experience anisotropic volume change which is an abrupt lattice contraction and expansion in a deeply charged state causing stress on inter-particle boundaries. These stress concentrations can then cause cracking at the grain boundaries which also allows electrolyte to enter the cathode particles and react with their internal surfaces.[19] Electrode growth measurement techniques including synchrotron CT scans have been able to show extensive micro-cracking and morphological changes that occur at the particle level in cathode materials over cycling. Figure 2.3 shows synchrotron CT scans for the cell degradation of an NMC622/graphite pouch cell, and the behavior that is affiliated with cathode micro-cracking.

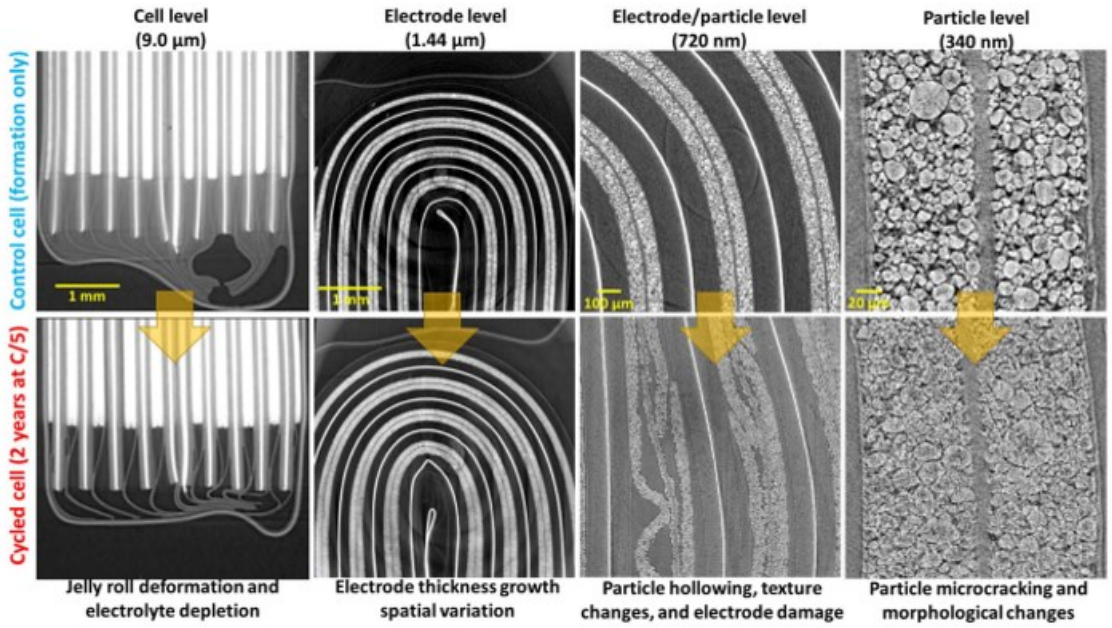

Figure 2.3: Cell degradation behavior (bottom labels) at multiple resolutions (top labels) for an NMC622/graphite pouch cell cycled for 2.5 years at C/5 from 3.0-4.1 V (bottom) compared to a control cell (top) that has only completed formation. This graphic comes Ref. 3.

The cathode micro-cracking can cause particles to swell which increases cathode layer thickness, and even can cause cathode delamination where the adhesion between the cathode coating and aluminum foil is lost. The particle micro-cracking

also leads to jelly roll distortion causing electrode damage as the stack is compressed into tight spaces near the current collector tabs. Overall, these effects can increase the total pore volume of the cathode layer leading to electrolyte depletion and possible cell failure.[3]

Silicon based negative electrodes for LIBs will undergo extreme volume changes of their micron-sized particles during lithiation which will cause continuous side reactions over repeated cycling at the silicon/electrolyte interphase. During cycling, electrolyte decomposition products will accumulate which will grow the SEI on the silicon particles, resulting in a loss of electrolyte and swelling which leads to a reduced performance in cycle life.[20] Figure 2.4 shows the primary Li-ion cell degradation mechanisms for silicon containing electrodes.

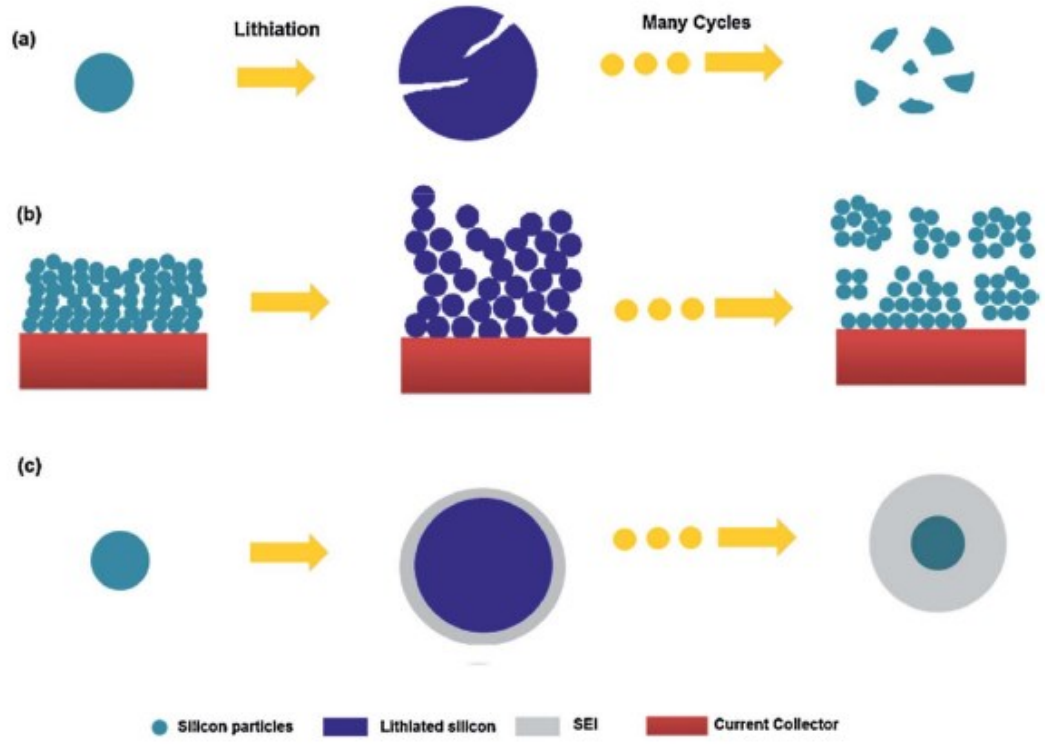

Figure 2.4: Li-ion cell degradation mechanisms for silicon-based anodes: (a) material cracking and pulverization, (b) electrode expansion and loss of electrical contact, (c) Ongoing SEI formation. The graphic is reproduced from Ref 21**.**

The repeated lithium insertion and de-insertion over cycling apply stresses within the silicon micron-sized particles leading to particle micro-cracking and eventually

pulverisation at the particle level. At the electrode level, the continuing expansion of the anode active material can lead to particle separation and a loss of electrical contact to the current collector and between particles. As discussed before, repeated cycling can increase the thickness of the SEI which will consume lithium from the electrolyte. These are all factors associated with volume change that can lead to rapid capacity fade.[21]

2.4.3 Active Mass Loss

The loss of active material for the positive and negative electrodes is another degradation mechanism for Li-ion cells. As discussed above, stresses can cause particles to crack, become detached from the rest of the electrode, and even delaminate from the current collector. Since lithium ions are stored in the active materials, the electrically disconnected materials will no longer be able to contribute capacity to the cell resulting in a decline in performance. The repeated expansion and contraction of the electrodes enhance the stresses which in turn increases cell degradation caused by the active mass loss.[2,22]

2.4.4 Gas Generation

The gas that is generated during cycling in Li-ion cells is a degradation mechanism that can cause serious problems, especially when at high voltages and temperatures. There are many researchers that study the electrochemical reactions that lead to gas generation and side products, as these processes are known to result in battery aging. For instance, experiments have shown that hydrogen gas can accumulate in the anode and increase the probability of thermal runaway in Li-ion cells. Parasitic reactions can lead to gas generation which can inflate the pouch cell contributing to battery degradation. As well, gaseous species have been shown to accelerate electrolyte decomposition (electrode dry-out) which can impact battery aging. Overall, the generation of gas during cycling can be detrimental to Li-ion cells in a multitude of ways that ultimately lead to capacity loss. Though, it is worth noting, that most gas generation occurs during the formation cycle, thus a proper formation procedure is required to improve battery

durability. Electrolyte additives are also commonly used to decrease the gas formation and improve the quality of the SEI.[23,24]

Chapter 3: Experimental Methods

3.1 Pouch Cell Assembly

There are three types of pouch cells with different electrode materials used in this work. There are two $LiNi_{0.83}Mn_{0.07}Co_{0.10}O_2$ (Ni83)/silicon-graphite (Si-G) cells with 20 and 10 wt% micron-sized silicon particles with 220 mAh nominal capacity, and $LiNi_{0.8}Mn_{0.1}Co_{0.1}O_2$ (NMC811)/natural graphite (NG) cells with 250 mAh nominal capacity. These pouch cells are 402035-size (40 mm long, 20 mm wide, 3.5 mm thick), have a flat wound electrode design, and were received dry without electrolyte from LiFUN Technologies (China). The pouch cells were opened in an argon-filled box and dried again under vacuum at 120°C for 14 h to remove residual water. Pouch cells were filled with 0.85 ml electrolyte, and vacuum sealed at -90 kPa gauge pressure in an argon-filled box.

All cells were charged to 1.5 V and held at constant voltage for 15 h to ensure wetting of the electrode pores with electrolyte, and to avoid dissolution of the negative electrode Cu current collector. The cells were then charged to 4.2 V and back down to 3.0 V at C/20 on a Maccor Series 4000 test system at a formation temperature of 40°C. To force evolved gas generated during formation out of the jelly roll, the cells were clamped with rubber blocks at 2 atm. Upon completion of the formation cycle, the cells were moved into an argon-filled glove box to be opened and the gas generated during formation was removed. The cells were then resealed.

3.2 Development of Laser Scanner

A laser scanning method was developed using two Gocator 2520 laser scanners from LMI Technologies Inc. for measuring pouch cell thickness. The two laser scanners (class 2) were fixed to a linear stage which is powered by a motor (Applied Motion Products, Inc.) to move the sensors along the y-axis as shown in Figure 3.1a. The motion is controlled by an automated software (Q Programmer) which dictates the speed, direction, and travel distance of the sensors. The two sensors move across the cell horizontally, recording 10,000 vertical line scan profiles per second (along the y axis) with 1920 data points per profile, as the cell

is held in position by a clamping mechanism shown in Figure 3.1b (see also Fig. A.1). There is one sensor on each side of the cell, and each sensor creates a line scan of data at a lateral resolution of 15 µm (x axis) and a thickness resolution of 0.57 µm (z axis). As the sensors move together, they create multiple lines of data, and as a result both scanners create scan data for the entire top and bottom surface of the cell.

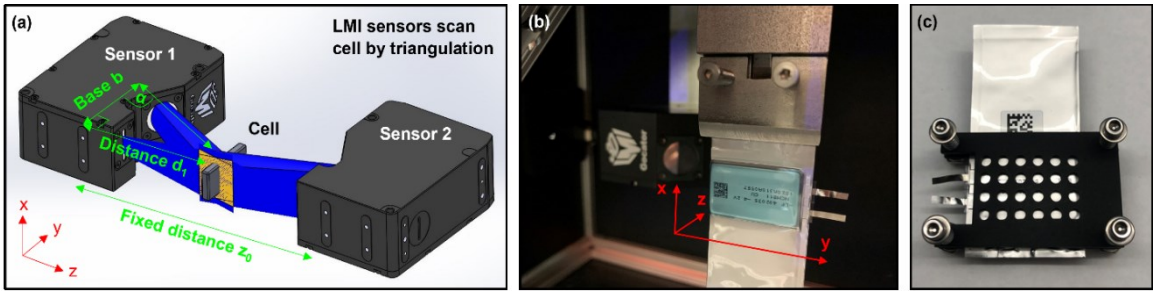

Figure 3.1: (a) Laser scanner setup with battery cell in the center and two laser scanners on each side. Laser scanners move on a motorized stage along the y-axis and scan the top and bottom surface of the cell. (b) 402035-sized pouch cell in laser scanner setup. A full scan of such a cell takes ~5 seconds. (c) Compression fixture for pouch cells allows operando laser scans during battery cycling with compressed cell stack. The holes expose the top and bottom surface of the cell.

The laser scanners are equipped with a built-in software which records the data points for the top and bottom surface of the cell by measuring the distance from the first sensor to the top surface of the cell, and the distance from the second sensor to the bottom surface of the cell (see Fig. 3.1a). This is done using a triangulation technique where the laser light shines (from the bottom component of the sensor that is parallel to the y axis) onto the surface of the cell at distance d_1, and the light is reflected to the receiver (the top part of the sensor) to create an angle α (the receiver calculates α based on proprietary information) as shown in Figure 3.1a. The distance b from the laser to the receiver is known, and the distance d_1 is calculated as follows:

$$d_1 = b \cdot \tan \alpha \tag{3.1}$$

There is a fixed distance z_0 between sensors 1 and 2, which is used along with the value of d_1 to record the surface data points of the top surface of the cell. The same process is used for the bottom surface of the cell using sensor 2.

The laser scanner method works in operando to record laser scans for the pouch cells periodically once per hour for each operando charge/discharge cycle. The data acquisition time (5 seconds) is negligible compared to the time of a typical C/10 operando cycle (20 hours). The cells were cycled at slow rates during operando to allow more time for lithium to intercalate graphite and alloy with silicon to achieve optimal swelling for the laser scanner to detect. More scans could be completed to obtain more data, though there are limitations with how much scan data the sensors can hold per operando cycle.

3.2.1 Thickness Measurements

The laser scanner records data points for the entire surface of the pouch cell; there are z values (thickness of the cell) for each x and y position recorded at a resolution of 0.57 µm that make up the data structure of the cell shown in Figure 3.2. The data structure is exported from the laser scanners' built-in software and a Python code (see Chapter A.2 in the Appendix) converts the surface of the cell into a color-coded thickness map (see Fig. 3.2a). The Python code also averages over the entire surface of the cell to calculate the average thickness value of the cell (see Fig. 3.2b). The code uses a specified range to perform the thickness calculation by selecting maximum and minimum z values to neglect parts of the cell that are not needed, e.g., the gas bag and tabs.

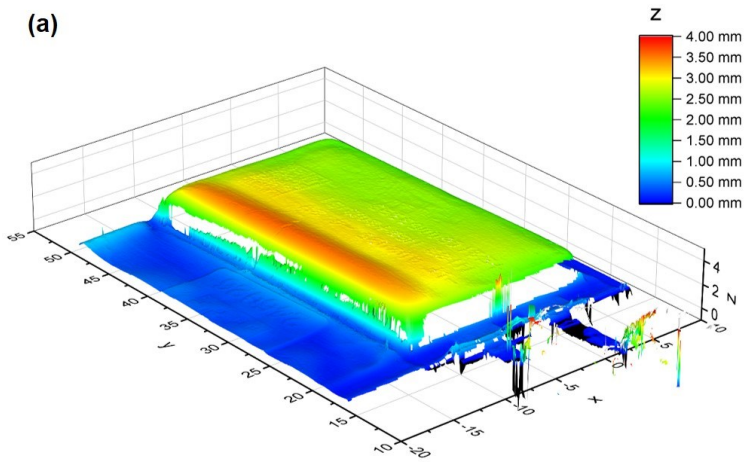

(b) **Data structure**

y/x	x1	x2	x3
y1	z11	z21	z31
y2	z12	z22	z23
y3	z13	z23	z33

Average thickness

$$z_{avg} = \Sigma(z_{ij})/(i_{max}*j_{max})$$

Figure 3.2: (a) 3D image of 402035-sized 250 mAh pouch cell as obtained from the laser scanner. (b) Data structure and equation for average thickness calculation.

3.2.2 Benchmarking

The laser scanner, a Mitutoyo linear gauge (see Fig. 3.3a), and calipers (see Fig. 3.3b) were used to measure the thickness of a big and small metal shim with uniform surfaces. The micrometer (see Fig. 3.3c) was used to measure the thickness of dry pouch cells which will be discussed in this section below.

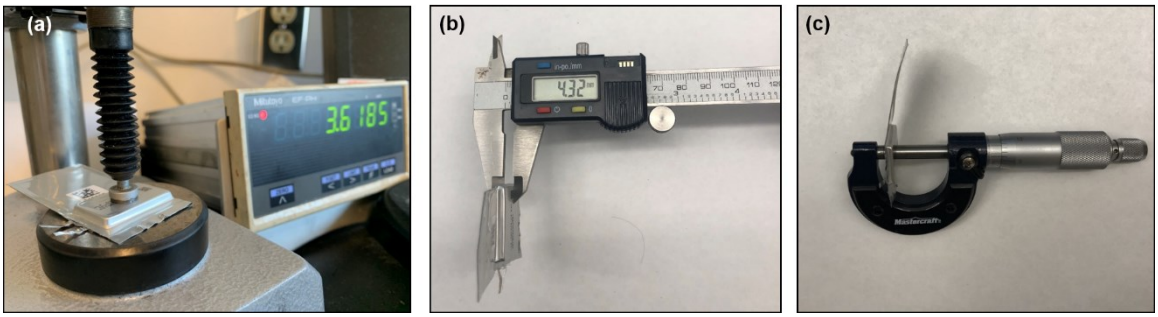

Figure 3.3: (a) Pouch cell in linear gauge for a thickness measurement. (b) Calipers are used to measure the thickness of one of the four sides of a pouch cell. (c) Micrometer is used to measure the thickness of one of 6 locations of a pouch cell.

Figure 3.4 demonstrates the uniformity of the shims with 3D and 2D color-coded thickness maps developed by the laser scanner.

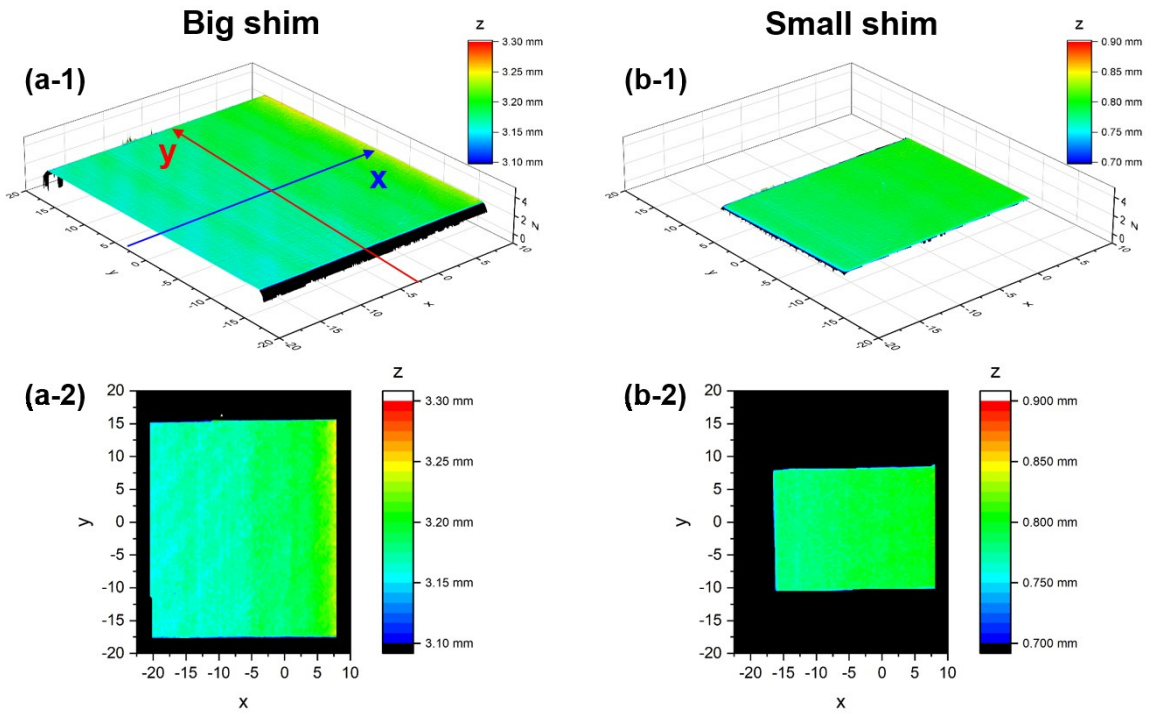

Figure 3.4: 3D scan (a-1) and 2D map (a-2) of big metal shim and a small metal shim (b).

Line scans were then generated by the laser scanner for both shims to map thickness change in the y-direction for a constant x-value (see Fig. 3.5a), and to map thickness change in the x-direction for a constant y-value (see Fig. 3.5b). The line scan thickness values recorded by the laser scanner align with the thickness values recorded by the conventional thickness measurements of the linear gauge and calipers.

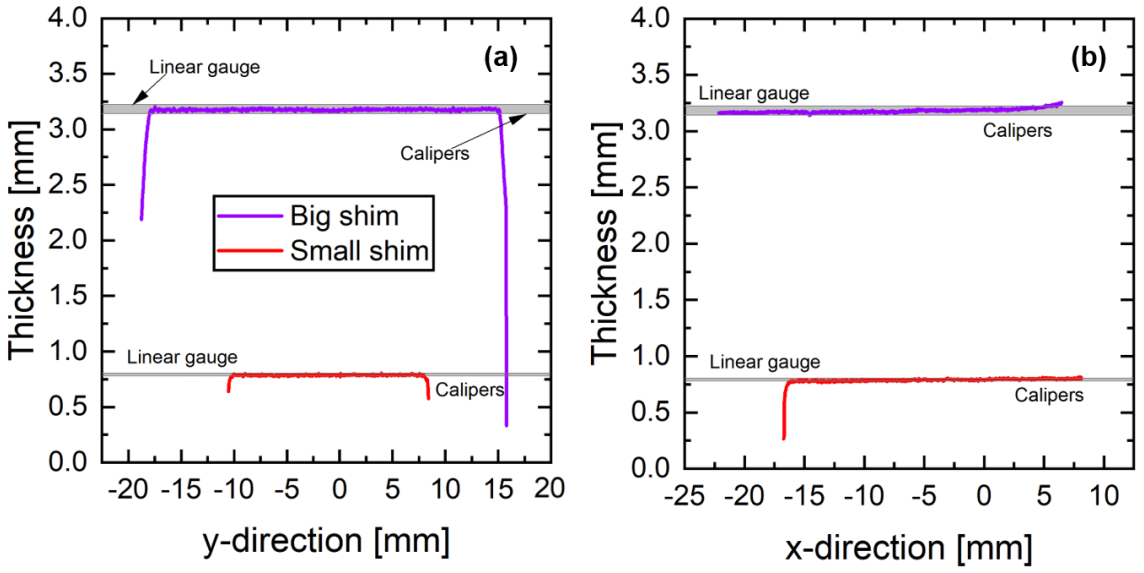

Figure 3.5: Line scans of shims in y-direction (a) and x-direction (b); see Figure 3.4a for how x- and y-direction are assigned. Grey bands show range of conventional thickness measurements with linear gauge giving the highest values and calipers (average of 4 measurements, one for each side) giving the lowest values.

Then, the overall average thickness values were recorded (see Table 3.1), and the laser scanner deviated from the conventional thickness measurements by -0.76-2.31%, giving confidence the laser scanner is an accurate technique for measuring thickness.

Table 3.1: Comparison of thickness measurements recorded by laser scanner relative to Calipers and Linear gauge. Deviations in percent relative to laser scanner measurements are shown in brackets.

Thickness [mm]	**Calipers**	**Linear gauge**	**Laser Scanner**
Big shim	3.14 (-0.62%)	3.223 (+1.97%)	3.159
Small shim	0.78 (-0.76%)	0.805 (+2.31%)	0.786

The laser scanner, linear gauge, and calipers were then used to measure the thickness of three 402035-size Li-ion dry pouch cells (LiFUN Technologies, China) with non-uniform surfaces. Three cell types with varying thickness were selected:

NMC811/copper, NMC532/graphite, and LFP/graphite. Figure 3.6 shows images for these dry pouch cells along with 2D and 3D color-coded thickness maps demonstrating the non-uniformity of these cells with discrete changes at the edges.

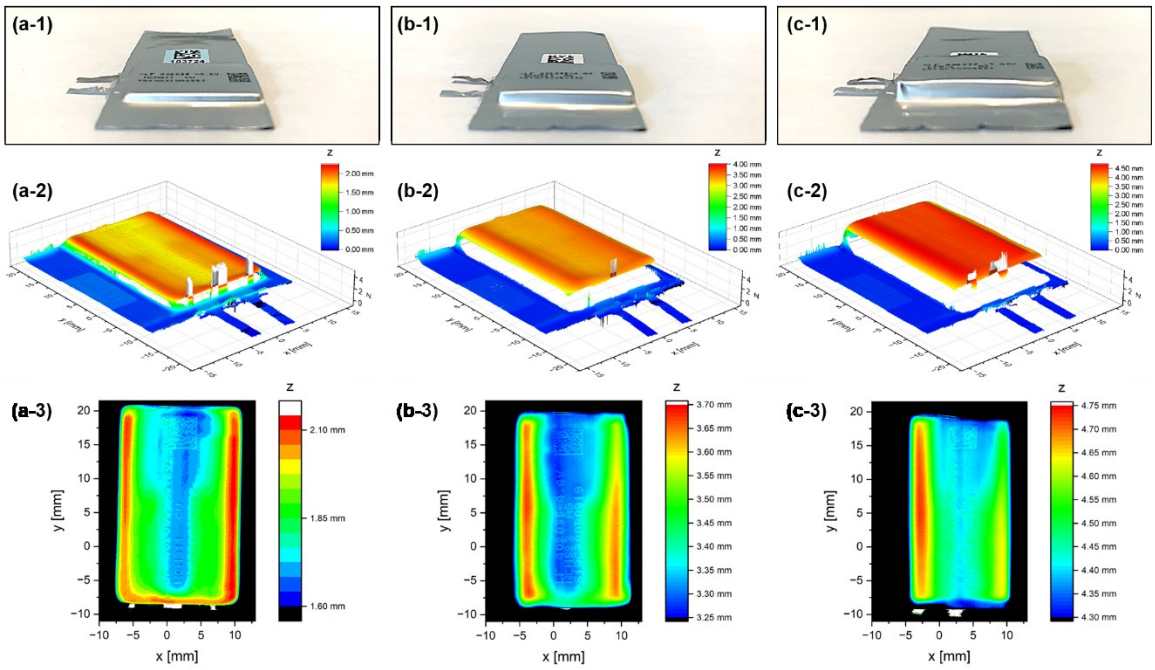

Figure 3.6: Photograph (top), 3D laser scan (middle), and 2D thickness map (bottom) of dry NMC811/Cu (a), NMC532/AG (b), and LFP/AG cells (c).

Line scans were then generated by the laser scanner in the x-direction for a constant y-value for these cells (see Fig. 3.7). The line scan thickness values recorded by the laser scanner align with the conventional thickness measurements at the edges of the non-uniform cells, demonstrating that the linear gauge and calipers are not measuring the true average thickness of the cells but picking up on elevated cell features.

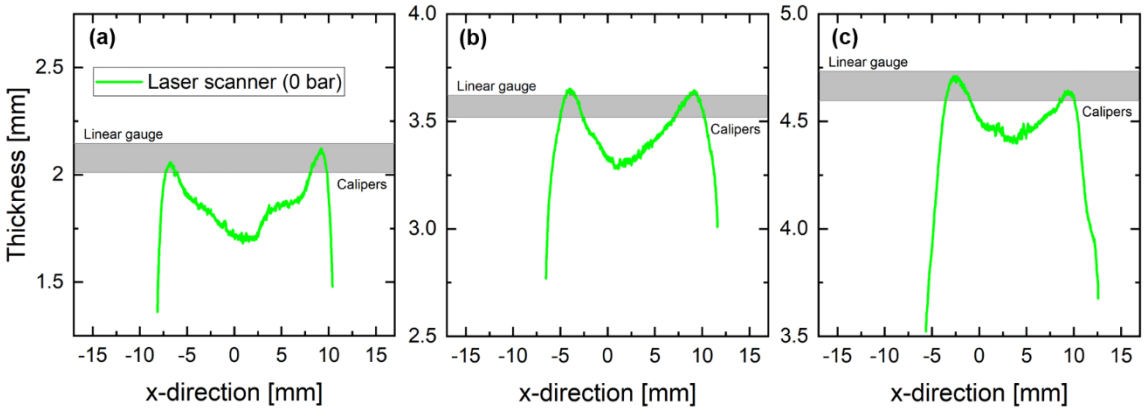

Figure 3.7: Line scans of dry NMC811/Cu (a), NMC532/AG (b), and LFP/AG (c) cells in x-direction. Grey bands show range of conventional thickness measurements with linear gauge giving the highest values and calipers (average of 4 measurements, one for each side) giving the lowest values.

For the linear gauge, the shims and cells were placed carefully onto a platform where the linear gauge takes a single point thickness measurement by applying pressure to the center point on the top surface of the cell. The calipers recorded the thickness values for one side of the uniform shims, and 4 values for each side of the non-uniform dry pouch cells to calculate an overall average thickness. The micrometer recorded 6 thickness values (3 each on the top and bottom of the cell spread evenly across) to calculate an overall average for the dry pouch cells. The measurements performed using the gauge, calipers, and micrometer are done by hand and there is some error with repeatability.

Figure 3.8 summarizes the thickness values recorded for three pair cells of each cell type with the different measurement techniques (including the laser scanner with and without compression at 2 bar). The laser scanner thickness values are consistently lower than the thickness values recorded by the conventional measurement tools (the micrometer is an exception). This is due to the laser scanner accounting for the non-uniform features of the pouch cells providing confidence that the laser scanner data is the most accurate.

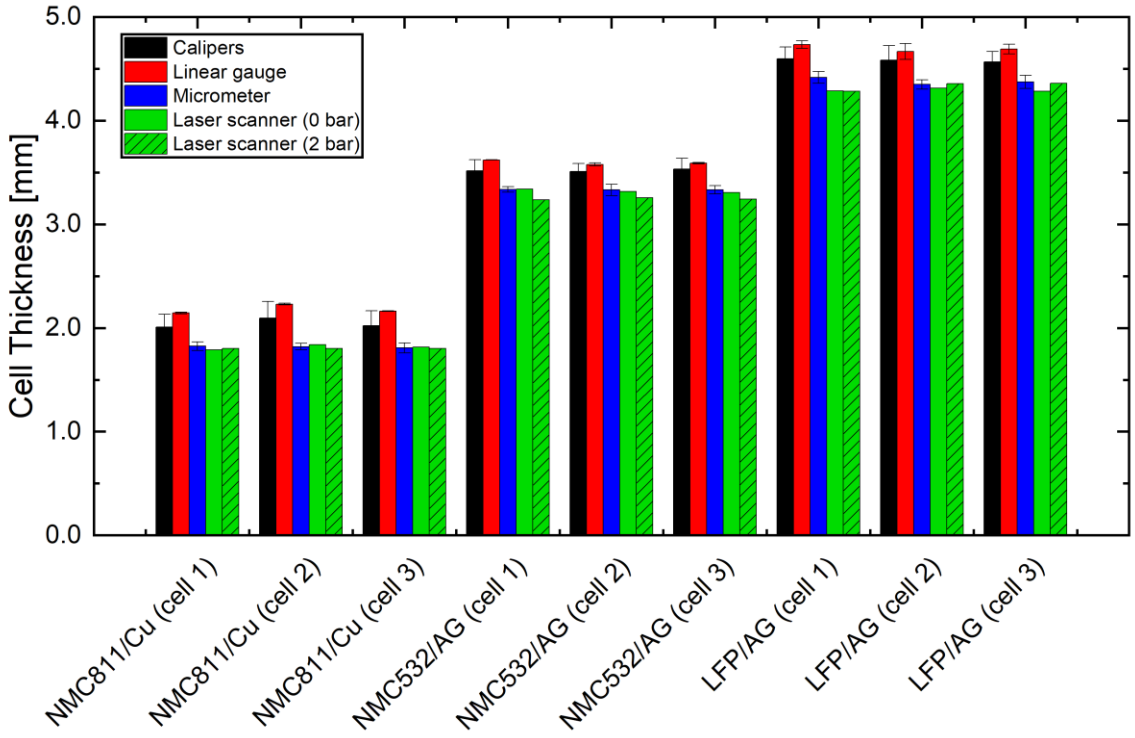

Figure 3.8: Thickness measurements of three sets of dry pouch cells with calipers (black), liner gauge (red), micrometer (blue) laser scanner 0 bar with no compression (green) and laser scanner with the compression fixture set to 2 bar (green hatched). Error bars refer to standard deviation of 3 repeat measurements for linear gauge, an average of 4 measurements for calipers (one for each side), and 6 measurements for micrometer (1 for 6 locations).

3.2.3 Compression Tool

Figure 3.1c above shows a compression tool designed to apply a pressure of 2 atm to the cell surface in order to push any gases generated during cycling into the gas bag and maintain good contact between the electrode layers, while allowing the laser scanners to record surface data through 3 mm holes evenly spaced 2 mm apart (see Fig. A.7). The tool consists of 2 aluminum plates painted black to reduce reflection of the laser light, which are tightened together with four 0.5-inch-long springs to a specified distance to achieve the required compression of 2 atm. The accuracy of a thickness measurement with the compression tool is within 1% of a regular scan (see Fig. 3.8). Note, optical glass or quartz were not used as a compression tool due to the refraction of the glass generated using the laser scanner. As well, glass could have potential issues such as impurities or cracking.

3.3 Large Format Automotive Pouch Cell

Figure 3.9 shows a large (270 mm long, 100 mm wide, 15 mm thick) pouch cell (SK Innovation) with stacked electrode/separator layers and a 60 Ah nominal capacity that was studied in this work using the laser scanner. The cell chemistry is medium-Ni/graphite, however details on active material composition, electrolyte formulation, and formation protocol are unknown. The cell was received with a low number of cycles and minimal capacity loss. The red and blue rectangles indicate the regions of the pouch cell that were scanned by the laser scanner. The regions do not cover the entirety of the cell due to the horizontal size restrictions of the laser scanner setup, the vertical field of view of the laser scanners, and the allowable capacity of scan data.

Figure 3.9: SK Innovation 60 Ah medium-Ni/graphite pouch cell. Areas mapped by laser scanner are indicated with red and blue rectangles.

3.4 Cycling

Cycle life testing was performed on Neware battery chargers where the cells were charged to upper cut-off voltages of 4.2 V and lower cut-off voltages of 3.0 V at constant current. The cells were cycled at a rate of C/10 during operando measurements on the laser scanner at 20°C (room temperature), and C/3 during long term cycling at 40°C with a C/20 check-up every 25 cycles.

In Section 4.1, Ni83/Si-G cells with 20% and 10% Si were cycled in operando on the laser scanner for 5 cycles without compression. In Section 4.2, the same cell

types were cycled in the compression fixture for 100 cycles with periodic operando cycles on the laser scanner on cycle 1, 25, 50, 75, and 100. In Chapter 5, the 250 mAh NMC811/NG cell and the 60 Ah medium-Ni/graphite cell were cycled in operando on the laser scanner; for the large cell, the laser scanner focused on the left corner position and the left middle position of the cell in separate back-to-back cycles (see Fig. 3.9).

3.5 Electrode Expansion Measurements

The primary techniques used in this work to measure volume expansion by means of thickness have been discussed in Section 3.2. Additional methods used in this work for volume and pressure will be discussed below.

3.5.1 Volume Measurements

The cells used in the first cycling experiment had their gas volume recorded using the Archimedes principle (using the apparatus shown in Ref. 25). Each cell was suspended in deionized water from a hook (a load cell attached to a balance) to measure the tension created by the suspended cell. The buoyant force acting on the suspended cell will change as the cell volume changes resulting in a change in tension, and thus a change in mass recorded by the balance $\Delta m_{balance}$. With density of the water, ρ_{fluid}, the change in volume of the cell Δv (gas generated) can be calculated:

$$\Delta v = - \Delta m_{balance} / \rho_{fluid} \tag{3.2}$$

A set of pair cells were placed in silicon mechanical pump oil using the same measurement principle and cycled without compression for 5 cycles. Using the density of the silicon oil, ρ_{fluid}, the change in volume during cycling is calculated.

3.5.2 Pressure Measurements

In-situ pressure measurements were made using a set of Ni83/Si-G pair cells that were fixed firmly into rigid aluminum holders so the expansion of the pouch cells would apply a force on the interior of the holder (using the same apparatus shown in Ref. 5). The force was measured using small load cells (model LCKD – OMEGA

Engineering) that were attached to DP25B-S-A strain gauge meters (OMEGA Engineering). The load cells were specifically placed between a force distributing plate and the inside wall of the aluminum holder. Gas generated during cycling does not impact the pressure measurements as the cell holder (which applies 2.23 atm of pressure to the cell) pushes the gas out of the jelly roll and into the pouch cell's gas bag. This set of Ni83/Si-G cells were put on a Neware battery charger system for formation and cycling without any degassing. The cells were charged to 1.5 V and held for 24 h; then they were cycled at a rate of C/3 with an upper cut-off voltage of 4.2 V, and a lower cut-off voltage of 2.8 V at 40°C. The formation cycle and checkup cycles which occurred every 20 cycles were done at C/20.

3.6 dV/dQ Analysis

Reference half-cell curves for differential voltage analysis were measured in 2325-sized coin cells. The full coin cells were made with $LiNi_{0.6}Mn_{0.2}Co_{0.2}O_2$ (NMC622) and NMC811 as the positive materials, and NG as the negative material. The coin cell design that offers high precision for Li-ion half cells including cell and spacer selection have been previously described.[26] The electrodes used for the full coin cells were the same electrode types described above for the third experiment (NMC622 was used for the large automotive pouch cell). The electrodes were opened in air, where one side of the double-sided electrodes was removed, and circular electrode disks were punched out, and heated under vacuum at 110 °C. The half-coin cells were then assembled in an argon-filled glovebox. Both cell types were cycled between 3.0-4.2 V at 40 °C and C/20 on the Ultra high precision coulometry (UHPC) system at Dalhousie University.[27] The second charge half cycle was used as the dV/dQ reference curves. The dV/dQ analysis was done using a free dV/dQ fitting software (see Ref. 28).

Chapter 4: Thickness Change in Silicon Containing Li-ion Cells

4.1 Short Term Cycling with no Compression

Figure 4.1 shows the operando thickness measurements for the first post-formation cycle of the 220 mAh Ni83/Si-G cells with 20% Si (a) and 10% Si content (b) without the use of the compression fixture, so there is no external pressure to the surface of the cells. The laser scanner can detect the increase in thickness during charge, and the decrease in thickness during discharge for both cell types in operando. The absolute (and fractional) change in thickness during charge (Δz_{charge}) is approximately similar for the 20% and 10% Si cells, and both cells experience an irreversible change in thickness (Δz_{irrev}) in the first post-formation cycle due to an incomplete SEI formation and particle micro-cracking, with the 10% Si cell having an even larger absolute (and fractional) irreversible thickness change than the 20% Si cell (see Fig. 4.1a-2 and b-2). One would expect that a larger silicon content results in more volume expansion, i.e., the 20% Si cell having a higher Δz_{charge} and Δz_{irrev} than the 10% Si cell. Both cell types have the same cathode loading and an adjusted anode loading (the 10% Si cell is 7.48 mg/cm^2 which is higher than the 20% Si cell at 5.06 mg/cm^2) to achieve a fixed N/P ratio of 1.1. Thus, the 10% Si cell is an overall thicker cell, but the particle distribution and uniformity of the electrode should be similar for both cell types. The cause for the larger irreversible thickness change of the 10% Si cell is currently unclear, but it could be an artefact from the lack of compression causing variability in the swelling of silicon containing cells.

The operando thickness profile is asymmetric between charge and discharge; it begins with a linear thickness increase during charge, but then shows a plateau at the beginning of discharge, during which the cell thickness does not change before it decreases linearly towards the end of discharge. The plateau is more pronounced for the 10% Si cell (see Fig. 4.1b-2). Louli et al. showed that silicon-containing cells have an asymmetric thickness plateau near top of charge (TOC), which results from the fact that in a silicon-graphite composite electrode, the graphite component delithiates first during discharge, which causes only minimal

overall thickness change due to graphite's relatively small particle level volume change (~10% for full delithiation). This minimal volume contraction is also cancelled out by the positive electrode expansion at the beginning of discharge resulting in an overall volume plateau. The silicon component only delithiates once most of the graphite capacity has been delivered. As soon as silicon starts to delithiate the overall thickness of the cell decreases rapidly, due to the enormous particle level volume change of silicon (~280% for full delithiation).[5]

During charge, the silicon and graphite particle level volume change contributes to the overall cell stack thickness change which is measured by the laser scanner. Calculation A.4.1 shows an estimated change in thickness based on the theoretical particle volume change and compares it to the laser scanner results to help further demonstrate the accuracy of the laser scanner technique as it works in operando. The calculation is performed by using the theoretical particle volume change to estimate the size of the silicon and graphite particles at maximum expansion, then predicting the amount of layers of particles in a single sided anode, then calculating the total change in thickness for all sides of the anode combined, and then the overall anode thickness change is used to predict the overall cell stack thickness change. The calculation helps put into context how much the particle volume change impacts the overall cell stack thickness change during charge, and it demonstrates that the predicted thickness change was indeed within accuracy of the thickness change recorded by the laser scanner while in operando.

For the 10% Si cell the thickness plateau is more pronounced, because more graphite capacity is available to be drawn from at the beginning of discharge. Based on the specific capacity of 372 mAh/g for graphite and a typical reversible capacity of 2319 mAh/g for silicon,[29] the graphite component in the silicon-graphite composite electrodes with 20 and 10% Si, delivers approximately 40 and 60% of the electrode's capacity, respectively (see calculation in A.4.3).

Calculation A.4.3 shows how much capacity is delivered by the silicon and graphite components to help further explain the thickness trends measured by the laser scanner. The calculation was performed by multiplying the mass of the silicon and

graphite components by their respective specific capacities. The calculation demonstrates that the graphite delivers more capacity in the cell with less silicon content which helps to further explain the plateau seen in Figure 4.1b-2.

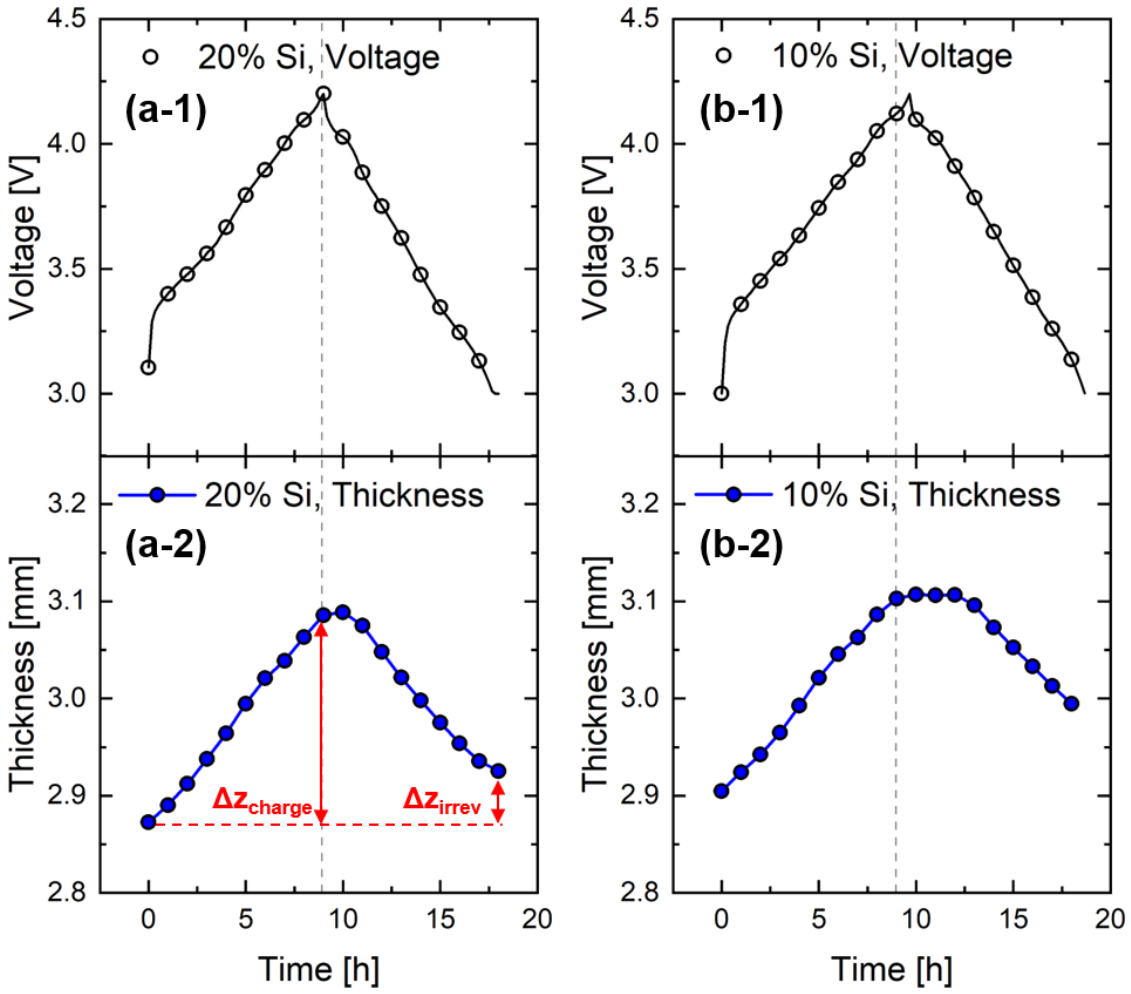

Figure 4.1: Operando thickness measurements **without compression fixture** for first post-formation cycle of 220 mAh Ni83/Si-G cells with 20% Si (a) and 10% Si (b). All data recorded at C/10 constant current charge and discharge between 3.0 and 4.2 V. Circles indicate the time of laser scans. One scan takes ~5 seconds. Arrows indicate thickness change during charge and irreversible thickness change within a complete cycle.

Figure 4.2 shows 2D thickness maps in the bottom of discharge (BOD) state at formation (a) for the same cells along with line scans during charge for cycle 1 in the y-direction (b), and in the x-direction (c). The laser scanner can map the

thickness distribution of the silicon containing Li-ion cells with the 2D color-coded thickness maps where most of the thickness change happens towards the left side near the gas bag due to the cell being less restrained in that area. The color-coded line scans demonstrate that the cell swells in a non-uniform way during the charge step. There is larger change in thickness across the y-direction of the cell surface with the largest Δz_{charge} value of 600 μm for the 20% Si cell. This could be due to the scan being taken at x = -5.71 which is closer to the gas bag. The change in thickness also decreases in the x-direction away from the gas bag which correlates with the 2D thickness map distribution. Figure 4.3 shows similar graphs for the discharge step. This data suggests that thickness mapping in uncompressed pouch cells with materials like silicon that lead to large thickness changes can be error prone if one uses localized thickness measurement tools, e.g., calipers or linear gauges. Since the thickness variations are very heterogeneous across the pouch cell surface, one needs to average over the entire surface, and even with the less constrained parts of the cell, in this case near the gas bag, since they swell more than other parts. Note that state of charge variation within the electrode as a function of distance from the current collector tabs are not an issue, since the cells are cycled at a slow rate of C/10 on the laser scanner, which is slow enough for any heterogeneities in lithium contraction to even out.

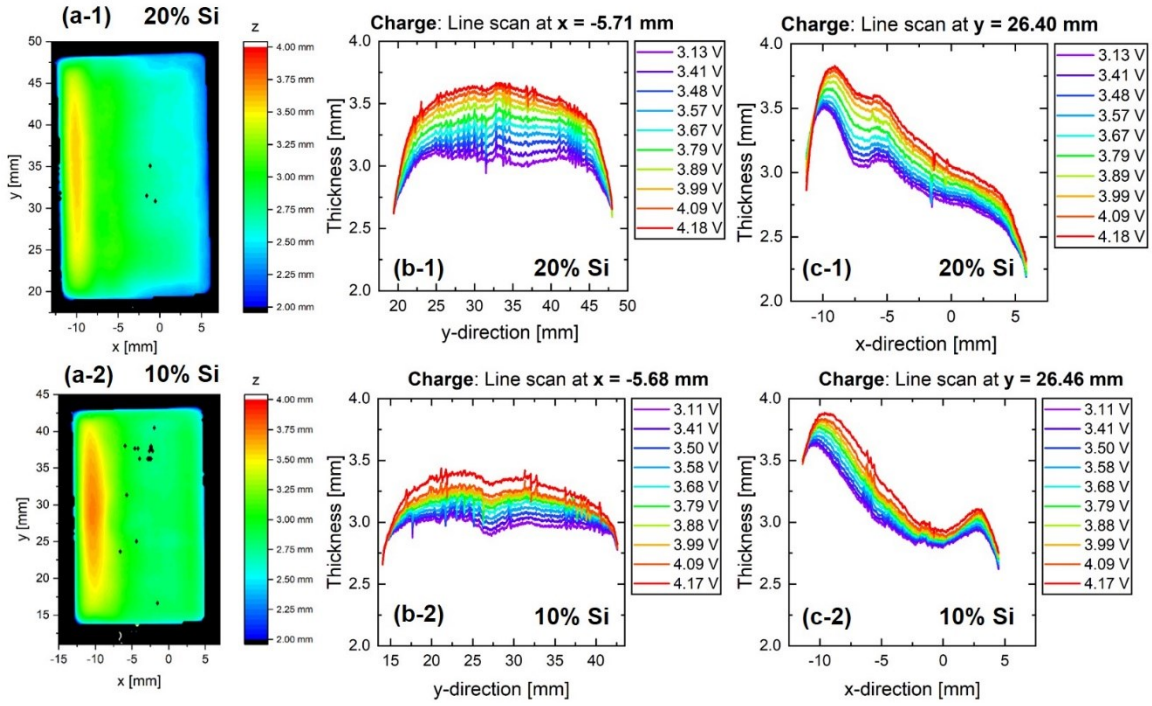

Figure 4.2: BOD formation 2D thickness maps for Ni83/Si-G cells with 20% Si (a-1) and 10% Si (a-2) **without compression fixture**. Operando line scans in y-direction for 20% Si cell (b-1) and 10% Si cell (b-2) during the C/10 charge step of the first post-formation cycle, as well as similar line scans in x-direction (c-1 and c-2).

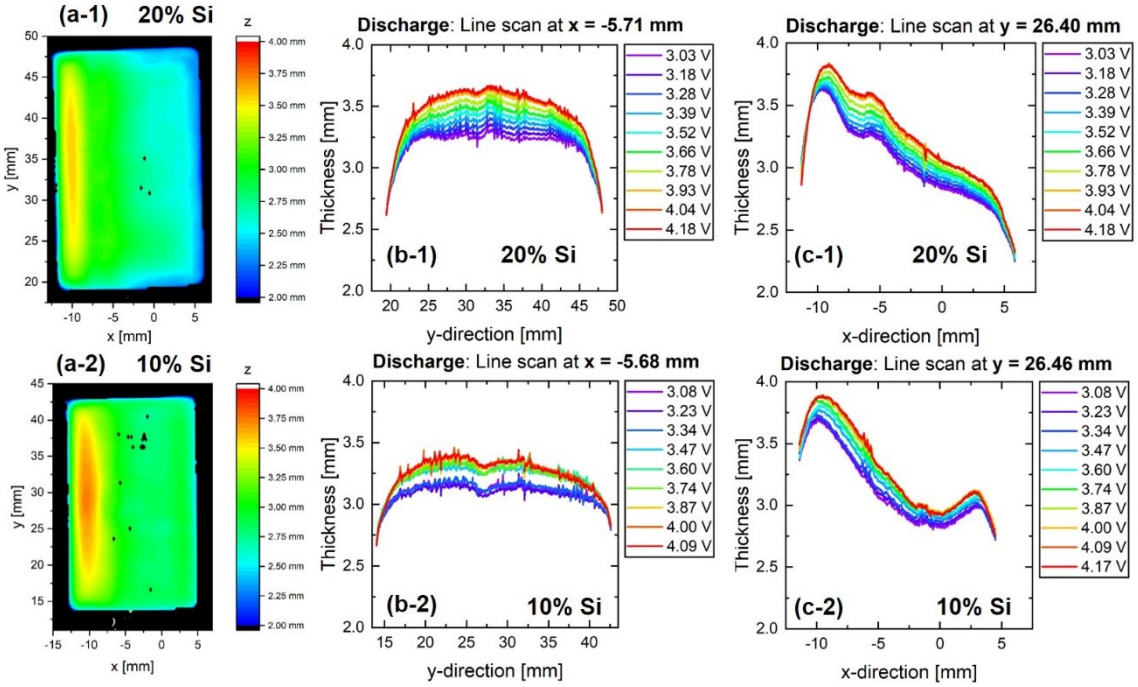

Figure 4.3: BOD 2D thickness maps for Ni83/Si-graphite cells with 20% Si (a-1) and 10% Si (a-2) **without compression fixture.** Operando line scans in y-direction for 20% Si cell (b-1) and 10% Si cell (b-2) during the C/10 discharge step of the first post-formation cycle, as well as similar line scans in x-direction (c-1 and c-2). For the 20% Si cell (b-1 and c-1), the final line scan was taken at 3.03 V. For the 10% Si cell (b-2 and c-2), the final line scan was taken at 3.08 V, i.e., shortly before the cells were full discharged.

Figure 4.4 shows a line scan comparison for the BOD formation cycle (purple) and BOD cycle 1 (red) for the same cells in the y-direction (a) and the x-direction (b). Ideally, the line scans would exactly overlap in each position for a cell with a fully reversible thickness change profile. The line scans in Figure 4.4 show a much larger thickness at BOD cycle 1 especially for 20% Si (see Fig. 4.4a-1 and 4.4b-1) demonstrating the irreversibility of these cells in the first post-formation cycle, where the SEI formation is not completed yet. Irreversible processes like uncontrolled interphase growth, electrode delamination or gas generation can lead to such a gap between the formation and cycle 1 BOD line scans. These cells were degassed after formation and do not produce any gas during the laser scanner measurement (see Fig. 4.5a), so gas generation should not be a factor. Furthermore, there is only minimal capacity loss (5.24 mAh and 3.48 mAh for 20%

and 10% Si respectively), which excludes any significant delamination that would be correlated with active material loss and capacity fade. Thus, uncontrolled SEI growth is a likely explanation for the gap between the line scan profiles. Operando pressure measurements have shown that SEI growth at the negative electrode can cause irreversible pressure increase.[30] While the thickness of typical SEI layers are ranging from tens to hundreds of nanometers, the large volume change of silicon particles can lead to fresh surfaces for electrolyte decomposition and an increased rate of SEI growth at the silicon/electrolyte interface well past this thickness range.[31] Note that the absence of compression in these cells can exacerbate irreversibility, especially when cells go through a large thickness change over the course of one charge/discharge cycle. Another factor that can influence the gap between the thickness profiles is the exact time of the periodic laser scans. Data is taken every 1 h, so there is a chance the cell is not measured in the fully discharged state (3.0 V) at cycle 1, but slightly before. Here, the final lines scan at BOD cycle 1 were measured at 3.03 V for the 20% Si cell and at 3.08 V for the 10% Si cell. The initial line scan at BOD formation was recorded at 3.13 V and 3.11 V for the 20% and 10% Si cell, respectively, due to voltage relaxation during the transfer of the cells from the formation system to the laser scanner.

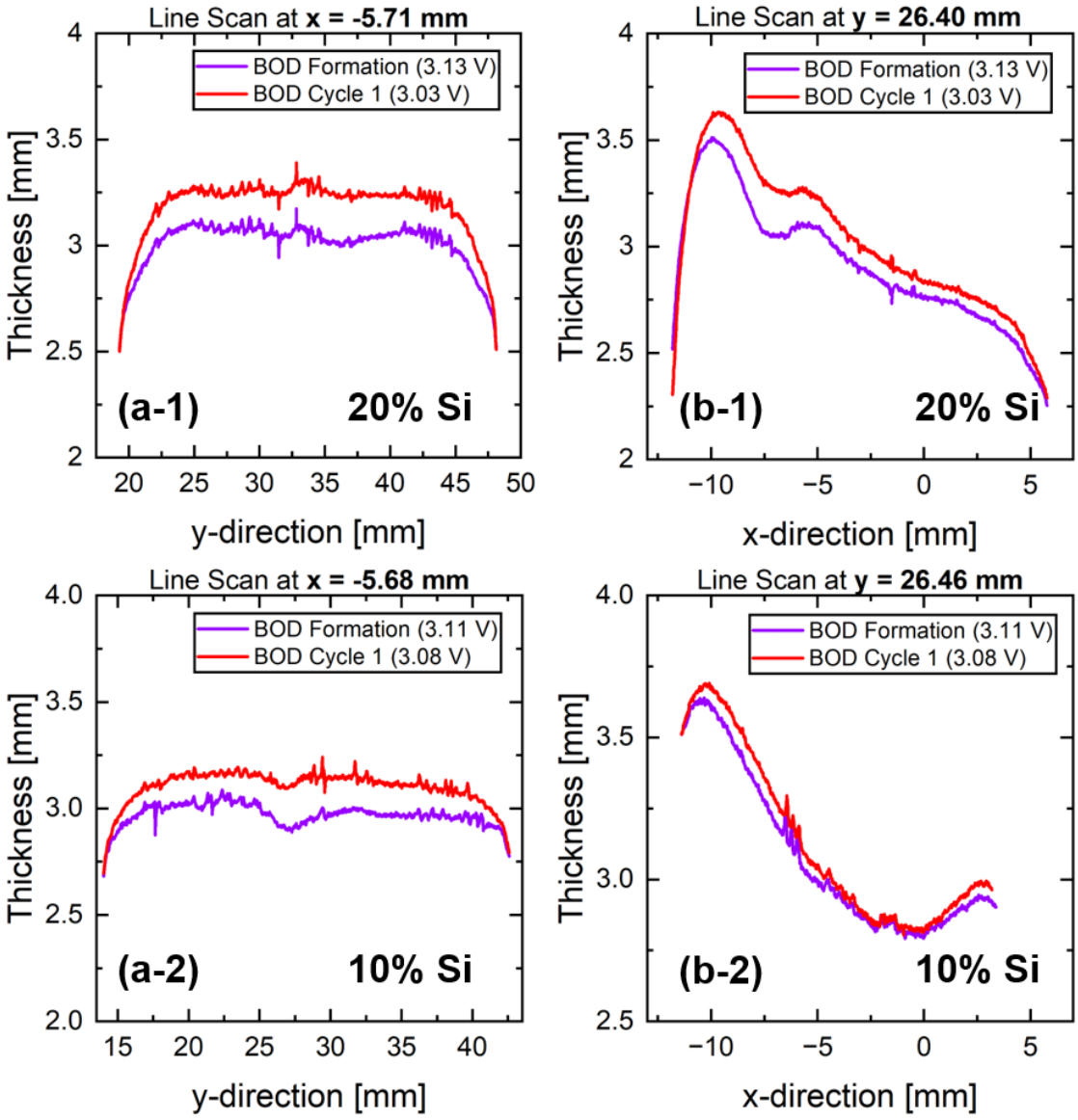

Figure 4.4: BOD formation (purple) and BOD cycle 1 (red) line scans for the first post-formation cycle at C/10 **without compression fixture** of Ni83/Si-G cells with 20% Si (a-1 and b-1) and 10% Si (a-2 and b-2) in y-direction (left side) and x-direction (right side). For the 20% Si cell (a-1 and b-1), the initial line scan was taken at 3.13 V instead of the nominal 3.0 V at the full discharged state due to voltage relaxation between end of the formation cycle and beginning of the operando cycle at the laser scanner, the final line scan was taken at 3.03 V. For the 10% Si cell (a-2 and b-2), the initial line scan was taken at 3.11 V and the final line scan was taken at 3.08 V, i.e., shortly before the cell was fully discharged.

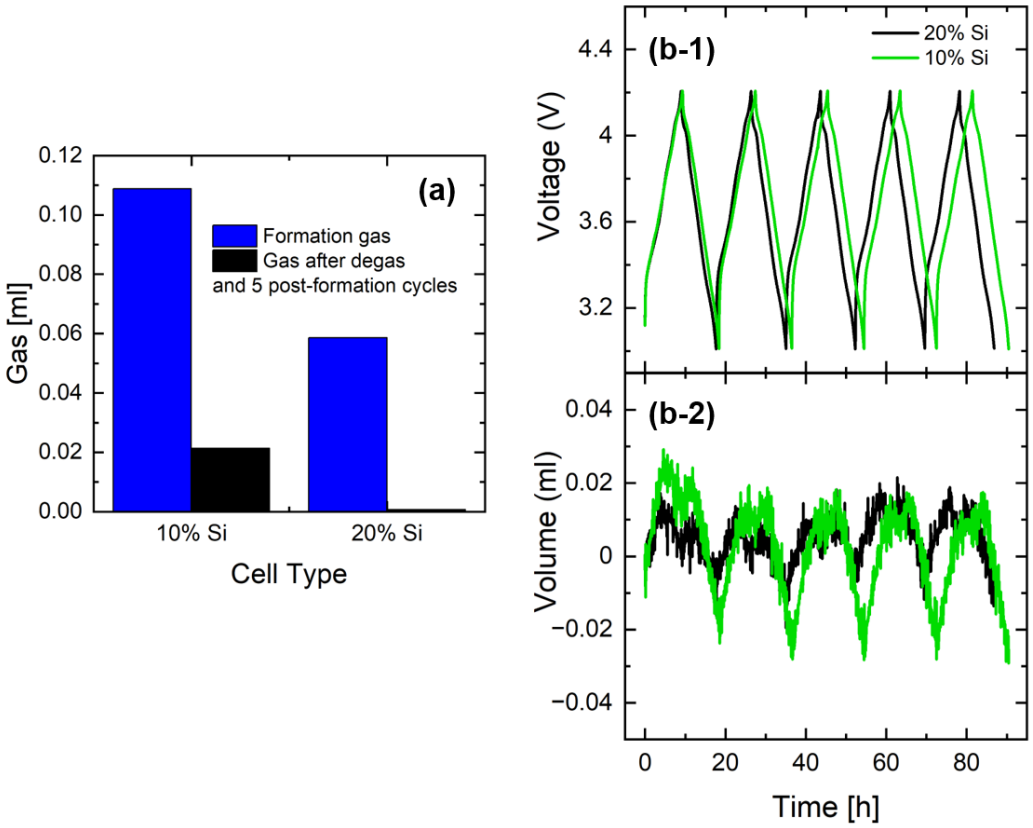

Figure 4.5: (a) Formation gas (blue) and gas volume after five operando cycles of Ni83/Si-G pouch cells **without compression fixture** at the laser scanner setup (black). (b-1) Voltage vs. time data recorded at C/10 constant current charge and discharge between 3.0 and 4.2 V. (b-2) In-situ volume measurements for an identical pair of uncompressed Ni83/Si-G pouch cells using Archimedes principle at 25°C (room temperature).

Figure 4.6 shows the coulombic efficiency (a), Δz_{charge} (b), and Δz_{irrev} (c) within one cycle for all 5 consecutive post-formation cycles of the Ni83/Si-G cells without compression fixture. The CE increases after formation and stabilizes at >99% in post-formation cycles 2-5. Δz_{charge} decreases after post-formation cycle 1 for the 20% Si cell and remains at ~5% for both cell types. Likewise, Δz_{irrev} decreases after post-formation cycle 1, but remains at ~1% irreversibility afterwards indicating ongoing SEI formation processes. The initial inverse relationship between CE and irreversible thickness change can be interpreted as incomplete electrode passivation after the formation cycle.[32] As the interphases in the cell mature, the CE increases and Δz_{irrev} decreases. However, since the CE is still far from unity

(not 1) and Δz_{irrev} is non-zero, there are continuous side reactions which lead to the accumulation of reaction products on the electrodes, and micro-cracking which can alter the geometry of particles and pore space, thus increasing cell thickness.[3,33] Figure 4.7 shows the thickness change percentage normalized to the initial formation cycle at bottom of discharge state (a) and the absolute cell thickness in mm (b) for all 5 consecutive post-formation cycles. These graphs further demonstrate the increase in thickness over cycling due to ongoing SEI formation processes**,** and micro-cracking for each cell type. For the above experiment which involved cycling the 220 mAh Ni83/Si-G cells with 20% Si and 10% Si content without compression fixture, it is important to show that gas generation during the 5 operando cycles is not a factor influencing the thickness measurements. The gas produced after 5 cycles on the laser scanner was measured using Archimedes principle and there was negligible gas produced (<0.2 ml) for both cell types (see Fig. 4.5a). To further demonstrate that gas generated was not a factor, a set of identical pair cells were cycled for the first 5 post-formation cycles under the same conditions, and in-situ volume measurements were recorded using Archimedes principle in which no noticeable gas generation was detected (see Fig. 4.5b). For these pair cells, it shows a slight contraction during the 5 cycles, though this is approximately zero and negligible. Consequently, the reversible thickness change (see Fig. 4.6b) is due to expansion of the electrode materials and the irreversible thickness change (see Fig. 4.6c) is due to the accumulation of reaction products at the interfaces, and the swelling of particles is due to intra-particle pore space caused by micro-cracking.

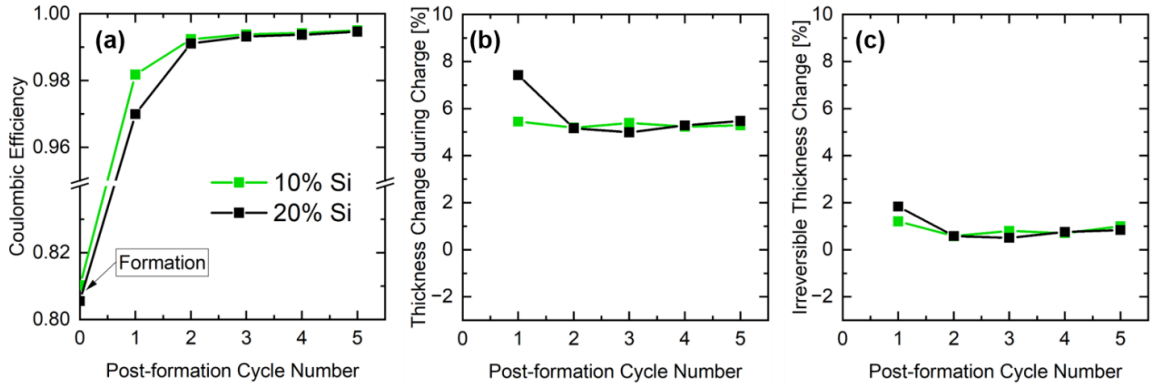

Figure 4.6: Coulombic efficiency (a), thickness change during charge (b), and irreversible thickness change within one cycle (c) for first 5 consecutive post-formation cycles at C/10 (a to e) of Ni83/Si-G cells with 20% Si (black) and 10% Si (green) **without compression fixture.** Note that the 10% Si cell is a duplicate cell and not identical to the cell shown in Figure 4.1.

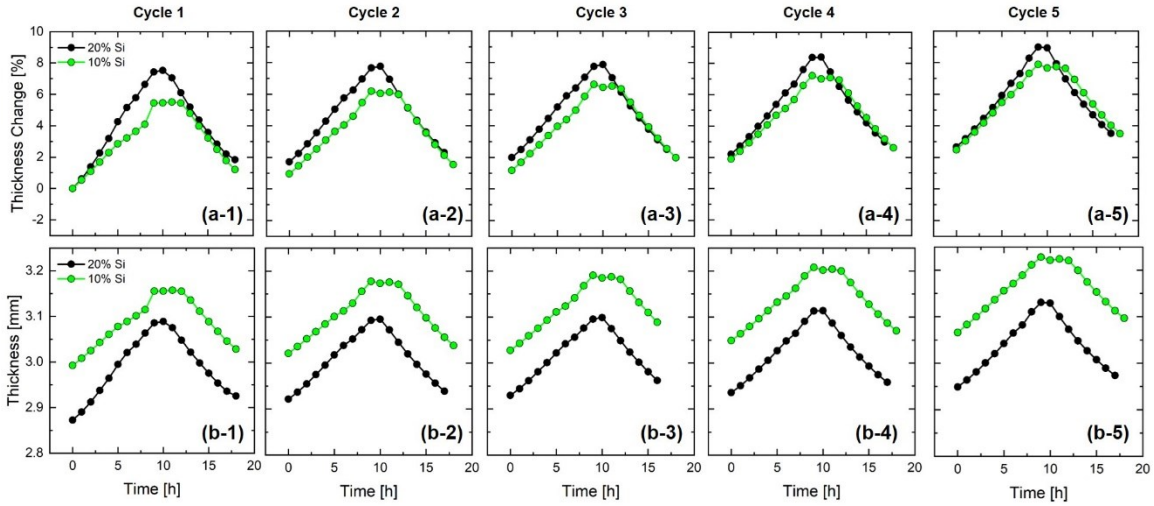

Figure 4.7: Normalized thickness change (a) and absolute thickness change (b) within one charge/discharge cycle for first 5 consecutive post-formation cycles at C/10 (a to e) of Ni83/Si-G cells with 20% Si (black) and 10% Si (green) **without compression fixture.** The thickness change for each post-formation cycle is normalized to the initial formation BOD state, since all cycled directly follow one another. Note that the 10% Si cell is a duplicate cell and not identical to the cell shown in Figure 4.1.

4.2 Long Term Cycling with Compression

This section will examine the thickness changes in aged Ni83/Si-G cells with 10 and 20% Si content in the negative electrode. Since gas generation is a known failure mode in long-term cycling of cells with relatively high Si content,[34,35] the following experiments use the compression fixture (see Fig. 3.1c) for applying pressure to the surface of the cells, pushing any gases generated during cycling into the gas bag. Figure 4.8 shows the discharge capacity (a), normalized discharge capacity (b), and normalized voltage hysteresis (c) for 100 cycles of the 220 mAh Ni83/Si-G cells with 20% Si (black) and 10% Si (green). These cells are cycling in their respective compression fixtures on a Neware system at 40°C but are periodically moved to the laser scanner for operando cycles at room temperature. In this process the cells are not taken out of their compression fixtures. The 20% Si cell lost 21% of its starting capacity after 100 cycles, which is more than the 10% Si cell with 16% capacity loss (see Fig. 4.8b). There was also a larger increase in voltage polarization for the 20% Si cell. Accelerated capacity loss and voltage polarization can be due to the larger silicon content resulting in more volume expansion of the negative electrode, fracture and rebuilding of the SEI layer, and thus faster consumption of the cyclable lithium inventory.[30,36]

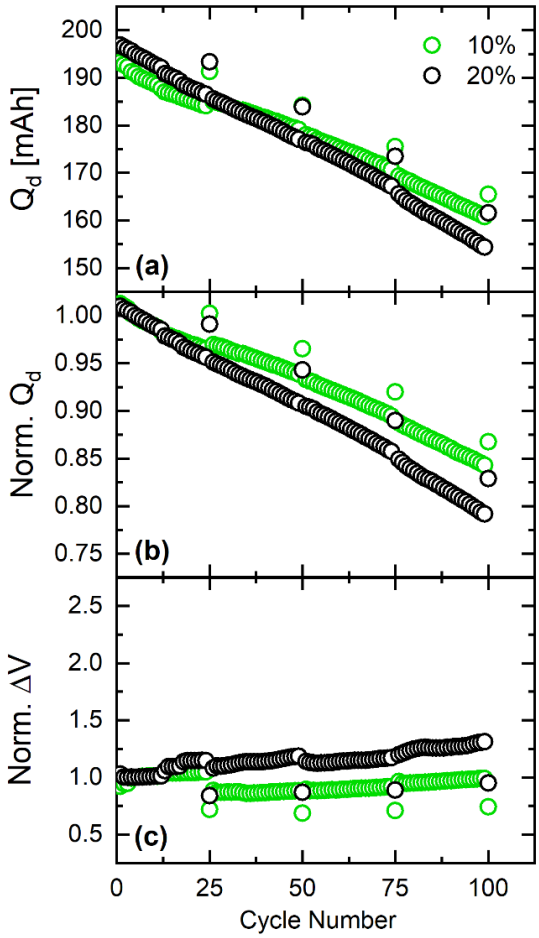

Figure 4.8: Discharge capacity (a), normalized discharge capacity (b), and normalized voltage hysteresis (c) versus cycle number for 220 mAh Ni83/Si-G cells with 20% Si (black) and 10% Si (green) cycling in compression fixture between 3.0 and 4.2 V at C/3 and 40°C. All cells do a checkup cycle at C/20 and an operando cycle at C/10 at the laser scanner setup every 25 cycles. The electrolyte is a dual lithium salt with no additives in EMC:FEC (8:2).

Figure 4.9 shows the operando thickness measurements for the first post-formation cycle of the 220 mAh Ni83/Si-G cells with 20% Si (a) and 10% Si (b) content with the use of the compression fixture applying pressure to the surface of the cells. This data can be directly compared to Figure 4.1, which showed data for the same cells without the compression fixture. With the compression fixture, the laser scanner is still capable of detecting the increase in thickness during charge, and the decrease in thickness during discharge for both cell types in operando. The absolute (and fractional) Δz_{charge} is now larger for 20% Si than for 10% Si,

which is expected since the Si component in the negative electrode should be the largest contributor to thickness change. The thickness change profile for both cells is much more reversible than without the compression fixture (see Fig. 4.1); though both cells show a slightly negative Δz_{irrev} of -14.17 µm and -20.61 µm for 20% Si and 10% Si, respectively. It is currently unclear what the source of this small thickness contraction is; some researchers report improved compaction of the negative electrode due to rearrangement of particles after the first cycles.[31,37] It is also possible in the early stages of cycling that the highly porous structure of silicon containing cells and a self-healing binder can accommodate the volume expansion from particle cracking.[38] Another possibility is the exact timing of the laser scans, note that the starting voltage is higher due to voltage relaxation after formation than the discharge voltage (see Fig. 4.9a-1 and b-1). As explained above, the asymmetry of the operando thickness profiles results from the graphite component in the composite electrode being delithiated first on discharge causing a small volume contraction that is cancelled out by the positive electrode expansion, and the silicon component only being delithiated afterwards causing large volume contraction. Again, the 10% Si cell shows a longer thickness plateau at the beginning of discharge (see Fig. 4.9b-2), since more graphite capacity can be delivered in this cell than in the 20% Si cell.

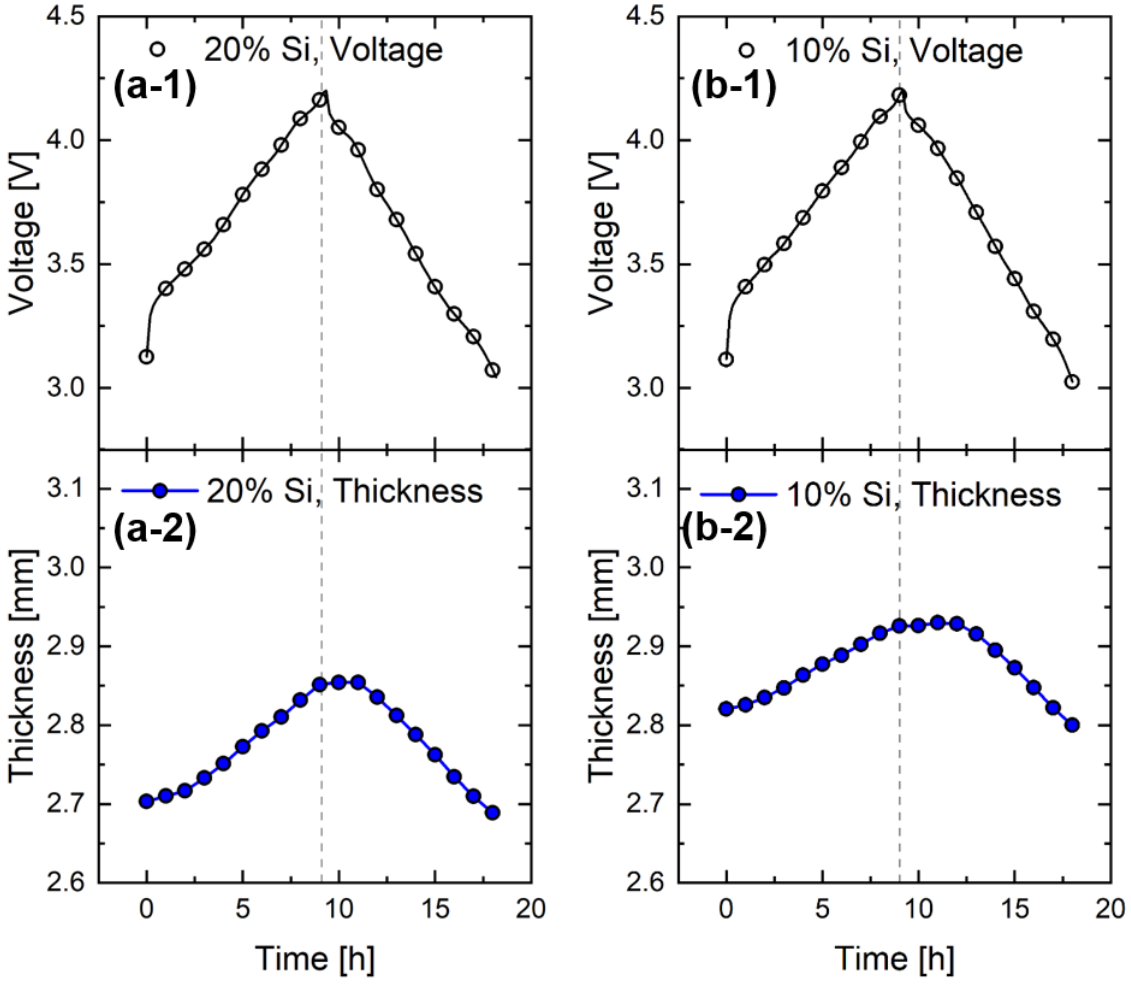

Figure 4.9: Operando thickness measurements **with compression fixture** for first post-formation cycle of 220 mAh Ni83/Si-G cells with 20% Si (a) and 10% Si (b). All data recorded at C/10 constant current charge and discharge between 3.0 and 4.2 V. Circles indicate the time of laser scans. One scan takes ~5 seconds.

Figure 4.10 shows the coulombic efficiency (a), Δz_{charge} (b), and Δz_{irrev} (c) within one cycle for post-formation cycles 1, 25, 50, 75, and 100. The CE increases after formation, reaches a maximum between cycle 25-50 and slightly decreases afterwards indicating a higher rate of parasitic reaction in later cycles. Δz_{charge} decreases after post-formation cycle 1 and remains similar afterwards for both cell types before slightly decreasing in cycles 75 and 100. As expected, the 20% Si cell has a higher change in thickness during charge than the 10% Si cell. For both

cell types, Δz_{irrev} increases from the negative values observed in post-formation cycle 1 (see Fig. 4.9) and is only slightly above 0% in the following cycles, indicating little irreversibility. Note that the data in Figures 4.6 and 4.10 cannot be directly compared, since the former shows fresh cells over only the first 5 post-formation cycles without compression and the latter shows more mature cycles of aged cells with compression. Figure 4.11 shows the thickness change percentage and the absolute thickness change for post-formation cycles 1, 25, 50, 75, and 100 of the aged cells. The thickness change percentage graphs (see Fig. 4.11a) corroborate the trends in Δz_{charge} and Δz_{irrev} described above; note that they are essentially the raw data of what is shown in Figure 4.10b. The absolute thickness graphs (see Fig. 4.11b) help determine the stack thickness growth over cycling, which will be discussed in Figure 4.12 for each cell type.

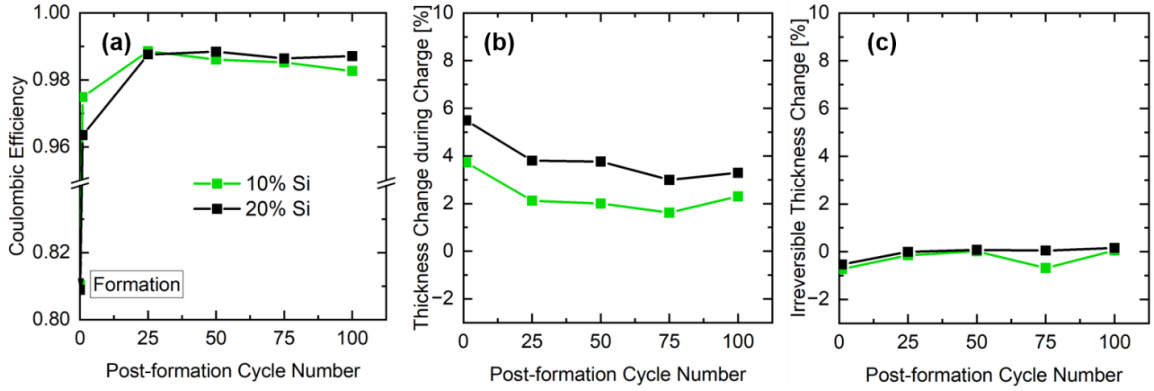

Figure 4.10: Coulombic efficiency (a), thickness change during charge (b), and irreversible thickness change within one cycle (c) for the 1st, 25th, 50th, 75th, and 100th post-formation cycle at C/10 (a to e) of Ni83/Si-G cells with 20% Si (black) and 10% Si (green) **with compression fixture.**

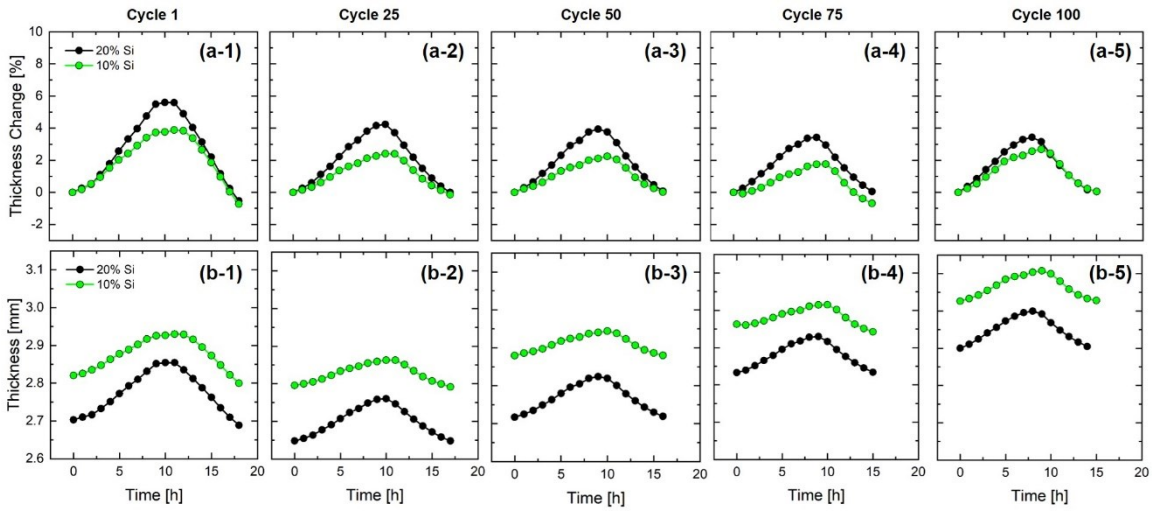

Figure 4.11: Thickness change (a) and absolute thickness change (b) within one charge/discharge cycle for the 1st, 25th, 50th, 75th, and 100th post-formation cycle at C/10 (a to e) of Ni83/Si-G cells with 20% Si (black) and 10% Si (green) **with compression fixture.** In between the operando cycles at the laser scanner, the cells were cycled at C/3 and 40°C at a Neware system. Cells were never taken out of the compression fixture. The thickness change is normalized to the BOD state of the respective cycle, since there are offline cycles at the 40°C Neware system in between the operando cycles.

Figure 4.12 shows the percentage change in stack thickness growth over cycling (a) and the change in average discharge pressure (b) for a set of pair cells using the pressure measurement setup shown in Reference 5 (see Fig A.2 for the absolute change in stack thickness growth). Similar trends are observed for stack thickness and pressure over cycling. As the cells age and lose capacity (see Fig. 4.8), the stack thickness and pressure first decrease over the initial ~20 cycles and then continuously rise for both cell types. As briefly mentioned above, the decrease in thickness and pressure for both cell types in the early stages of cycling may be due to a highly porous structure or the initial expansion of the negative electrode creating additional void space in the electrode where the micron-sized silicon particles can settle closer, and/or the micron-sized silicon particles fracture into smaller particles and settle in a more compact way.[31,37,38] After that, the continuous increase in both stack thickness and pressure is most likely due to the accumulation of reaction products on the individual electrode particles, first filling

up void space, and an increase in volume change can cause fracture of particles and polymer binder resulting in loss of electrical contact,[38] leading to an inevitable increase in thickness of each negative electrode layer.

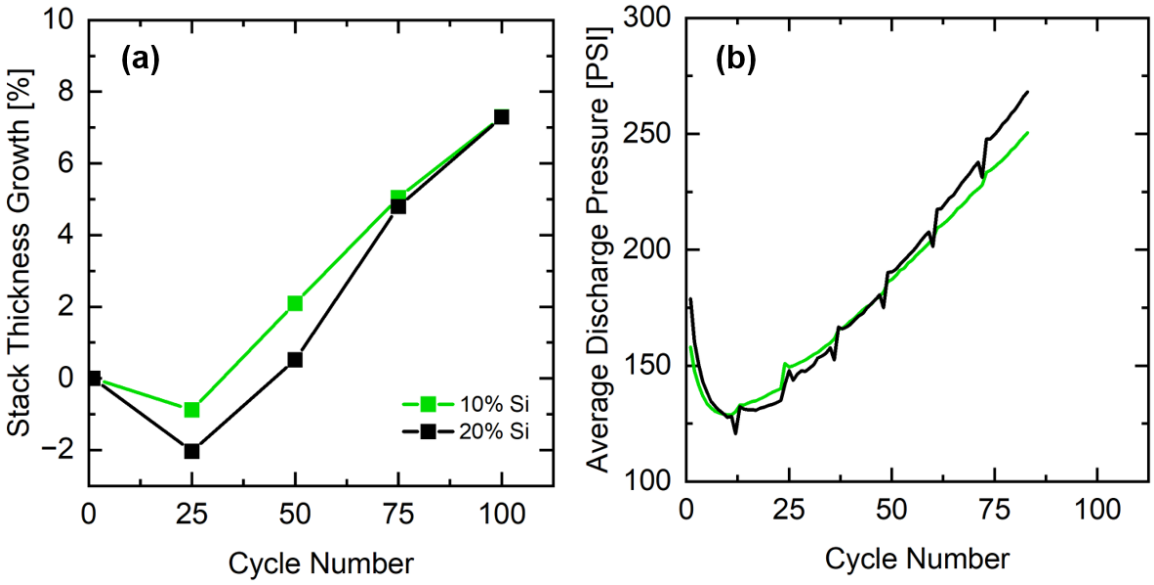

Figure 4.12: (a) Stack thickness growth versus cycle number for Ni83/Si-G cells with 20% Si (black) and 10% Si (green) **with compression fixture.** The thickness measurements are taken at the bottom of discharge state, and the change in thickness is normalized to the BOD formation cycle. (b) Average discharge pressure versus cycle number for similar cells cycling uniaxially constrained in aluminum enclosures with load cells to measure the pressure exerted by stack thickness growth.

Calculation A.4.2 provides an estimation of the cell stack thickness change experienced over the entire course of cycling to help further demonstrate the accuracy of the laser scanner system and its ability to make accurate measurements of cell volume change for long term cycling. The calculation is performed by predicting the volume of SEI species produced based on the known amount of capacity loss by the end of cycling. This predicted volume increase is compared to the calculated volume change of the anode based on the thickness change recorded by the laser scanner. The calculation demonstrates that the porosity of the cell plays a large role in limiting the amount of volume change that can be observed by the laser scanner. There are also too many limitations over

the course of long term cycling to provide a proper match of thickness predictions to the laser scanner measurements, thus more research on the theory of these limitations (see the limitations outlined in Section A.4.2) would need to be done to be able to provide accurate thickness predictions.

Since this long term study was performed using the compression tool, there is potential that the expansion of the cell stack over time could impact the pressure distribution applied to the cell surface by the compression tool. Calculation A.4.4 shows the maximum pressure change applied to the cell over the course of cycling and how it is a negligible difference that would not impact the overall long term results. The calculation is performed by using the maximum change in displacement of the compression springs due to the maximum thickness expansion of the cell stack, which in turn would alter the force applied by the springs and hence the overall pressure applied by the compression tool. The calculation shows that the springs do not exceed their permanent deformation point, thus the tool remained effective throughout the entire course of cycling implying the long term results would remain accurate.

Chapter 5: Thickness Change in Large Format Pouch Cell

This chapter demonstrates the utility of the laser scanning method on a large format automotive pouch cell (see Fig. 3.9 for a photograph of the cell).

5.1 Quantifying Cell Expansion and Distribution

Figure 5.1 shows 2D thickness maps of a 60 Ah medium-Ni/graphite cell for the left corner (a) and the left middle (b) positions. The graphs show that the laser scanner can map the thickness distribution of a large automotive format pouch cell in selected regions, and it can do so during cycling as the color-coded thickness maps show the thickness of the cell increase from BOD cycle n (n is an unknown low number of cycles) to TOC cycle n+1, and then decrease from TOC to BOD for cycle n+1 for both positions.

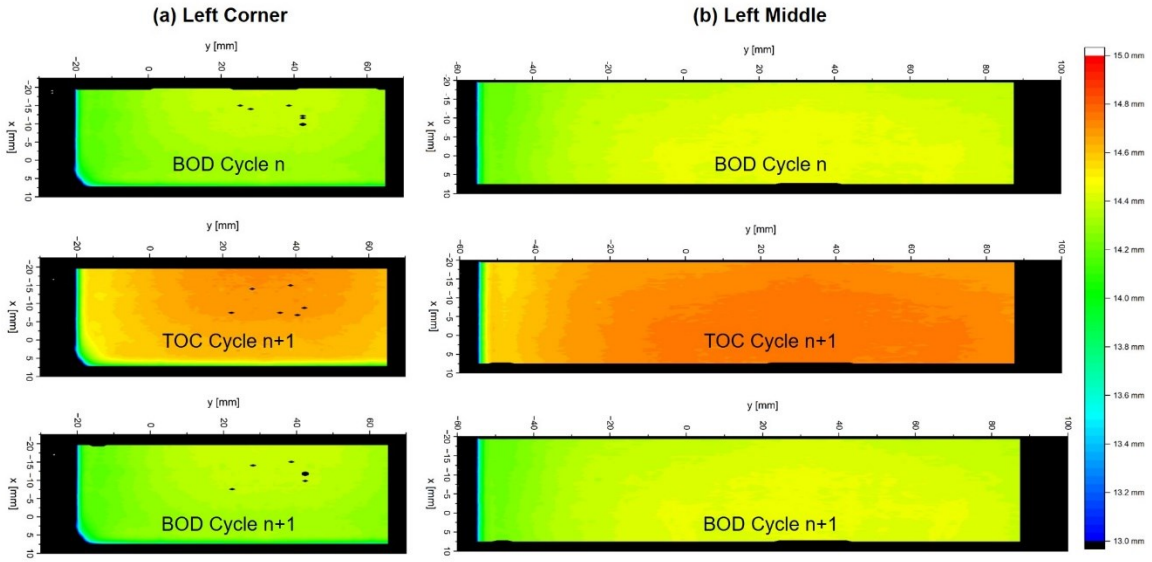

Figure 5.1: 2D thickness maps for the left corner (a) and left middle section (b) of 60 Ah medium-Ni/graphite pouch cell at BOD cycle n (top), TOC cycle n+1 (middle) and BOD cycle n+1 (bottom).

Figure 5.2 shows the operando thickness measurements over a single operando cycle for the left corner (a) and left middle (b) positions along with a comparative measurement of a 250 mAh NMC811/NG cell (c) without applying pressure to the surface of the cells. The laser scanner in operando can detect the increase in thickness during charge, and the decrease in thickness during discharge for the

large automotive cell (see Figs. 5.2a and b) and the small pouch cell (see Fig. 5.2c). It should be noted that these cells do not contain any silicon and thus show a distinct swelling profile that is governed by the graphite negative electrode and the medium to high-Ni positive electrode, while the linear swelling profile of the cells in Figures 4.1 and 4.9 were dominated by the silicon in the negative electrode. Figure 5.2 shows that the 60 Ah cell has a flat region after the first 3 h of charge and a steep rise in thickness towards the top of charge after ~6 h; by comparison the smaller 250 mAh cell (see Fig. 5.2c) shows a similar flat region and rise, but a thickness plateau at the top of charge. The flat region after ~3 h is due to the stage 2L to 2 transition in graphite lithiation.[30,39] The steep increase in thickness after ~6 h is associated with the transition of graphite lithiation from stage 2 to 1.[30,39] The interested reader can refer to Reference 30 for operando pressure measurements that show how volume change will vary depending on graphite phase transitions. dV/dQ analysis was performed for the 60 Ah commercial cell and the 250 mAh lab sized pouch cell (see Fig. A.3) to determine how much excess graphite capacity there was for both cell types; and it was found that both the lab and commercial cell have the same N/P ratio of approximately 1.19. The flat thickness profile at the top of charge for the 250 mAh lab sized pouch cell is likely due to NMC811 (and other high-Ni positive electrode materials) having more lattice contraction during top of charge.[40,41] The negative electrode is still increasing in volume, though the positive electrode contracts enough to balance it out. This implies the commercial cell is in the medium-Ni range, e.g., a NMC622/graphite cell. The thickness profiles shown here are symmetric as these cells do not contain any silicon.

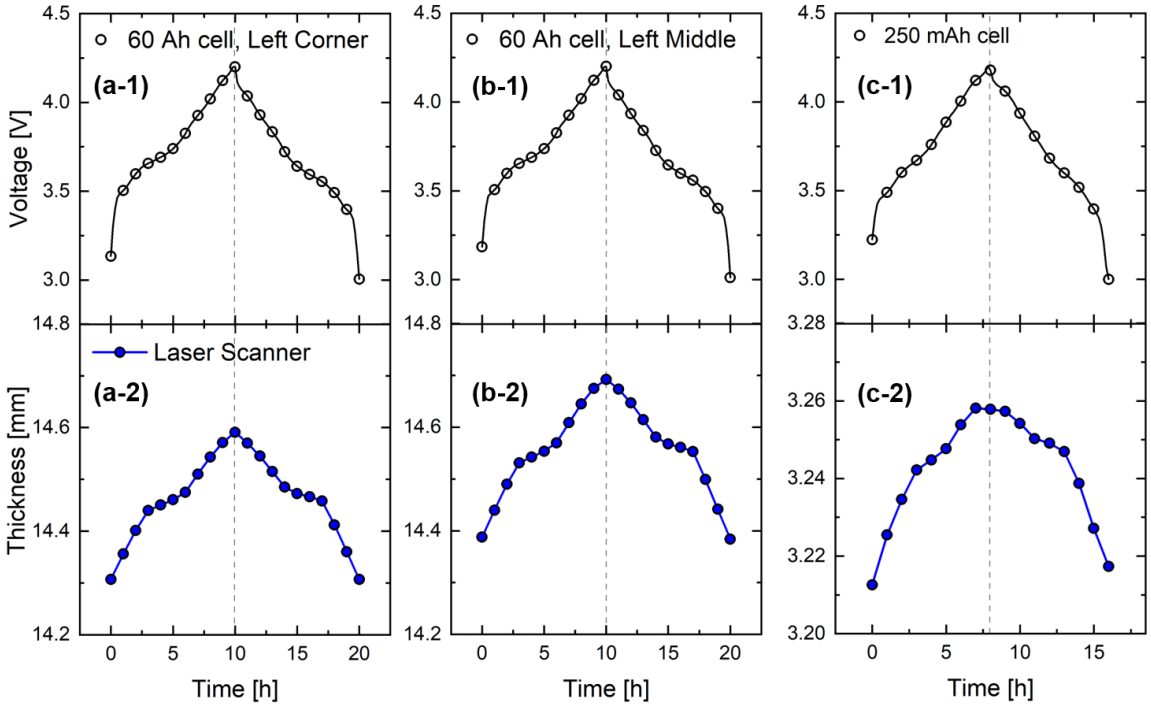

Figure 5.2: Operando thickness measurements for the left corner (a) and left middle section (b) of 60 Ah medium-Ni/graphite pouch cell. Comparative thickness measurement of full surface of 250 mAh NMC811/graphite pouch cell (c). All data recorded at C/10 constant current charge and discharge between 3.0 and 4.2 V. Circles indicate the time of laser scans. One scan takes ~5 seconds for the selected frame of the 60 Ah cell and the complete 250 mAh cell.

Figure 5.3a shows the volume growth of graphite when it is fully charged (SOC = 1) is 10%, and the plateau during the stage 2L to 2 transition that occurs is between 0.25 and 0.5 SOC. During this transition, both the 2L and 2 stage have lithium atoms intercalated into every second layer between graphene layers. Stage 2L is partially filled with lithium and transitions into stage 2 which is a phase that is fully filled with lithium. This transition does not involve lithium intercalating any other empty carbon layers, hence there is no volume growth during the stage 2L to 2 transition.[39] The relatively linear and large volume expansion of 280% for silicon (see Fig 5.3b) does not contribute to these silicon free cells as it did for the silicon containing cells described in Chapter 4. Hence, with no silicon in these cells, the stage 2L to 2 transition remains flat for these cells, and the overall swelling profile has more non-linearity. The volume contraction of the cathode is relatively small

during most of charge, though there is rapid contraction beginning at 0.75 SOC (see Fig 5.3c). This further explains the contraction seen for NMC811 at top of charge.

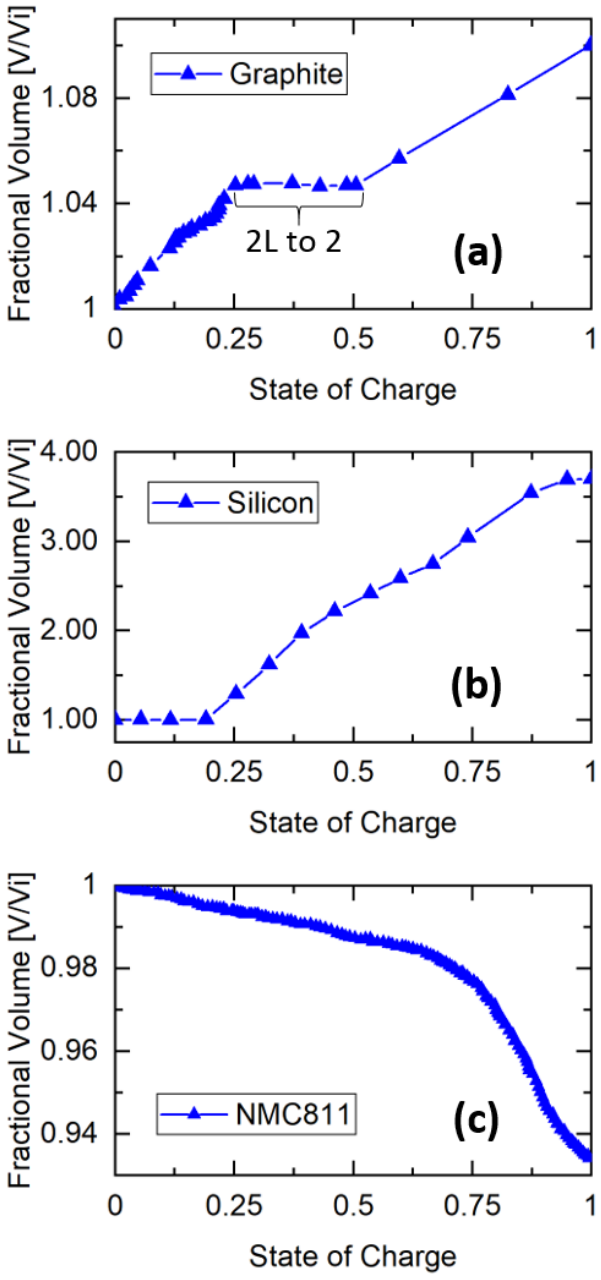

Figure 5.3: Fractional volume change during charge for graphite (a) silicon (b) and NMC811 (c). The data for (a) and (b) was adapted from Ref. 5. The data for (c) was adapted from Ref. 42.

Table 5.1 shows that the left corner of the automotive pouch cell swells slightly less than the left middle. This may be due to the cell stack being more constrained by the pouch foil at the corners (see Fig. 3.9). Furthermore, the small lab scale pouch cell swells less upon charge than the automotive pouch cell. This may be due to having more volume contraction at the TOC in the small cell with higher nickel content as explained above. Overall, though, the change in thickness during charge is quite similar for the two positions of the 60 Ah cell and the 250 mAh cell (see Table 5.1). This indicates that swelling studies performed on lab scale pouch cells are relevant for large automotive pouch cells, though many more studies are required to validate that the findings are transferable with a high degree of accuracy.

Table 5.1: Comparison of thickness change during charge for different sections of the 60 Ah pouch cells and the 250 mAh pouch cell.

Cell Type	Position	Thickness Change during Charge [%]
60 Ah medium-Ni/Graphite Pouch Cell	Left corner	1.99
60 Ah medium-Ni/Graphite Pouch Cell	Left middle	2.12
250 mAh NMC811/Graphite Pouch Cell	Full surface	1.42

5.2 Quantifying Cell Reversibility

Figure 5.4 shows a line scan comparison for the large 60 Ah cell (a and b) and the small 250 mAh cell (c) at BOD (purple) and at a BOD subsequent cycle (red) in the y-direction (top) and the x-direction (bottom). Interestingly, the swelling of the large 60 Ah cell in both positions as well as the swelling of the small 250 mAh cell are fully reversible as indicated by the complete overlap of the line scans in Figure 5.4. Clearly, these cells have matured interfaces potentially due to the absence of silicon in the negative electrode.

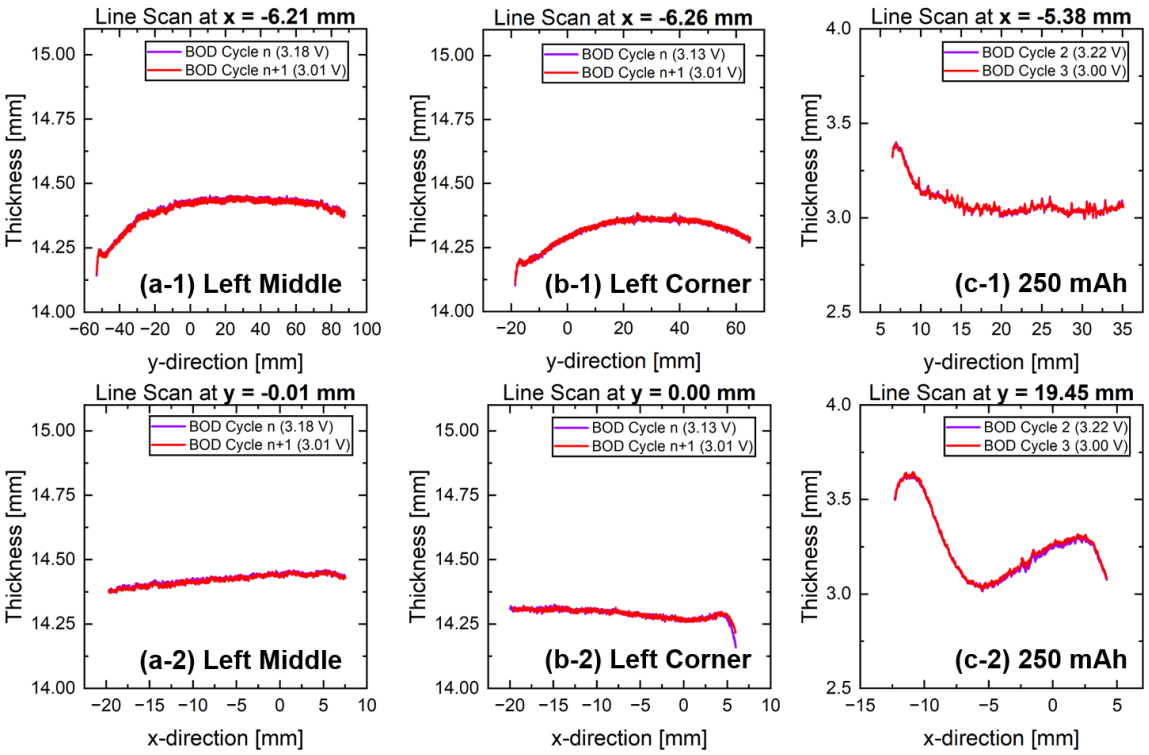

Figure 5.4: BOD cycle n (purple) and BOD cycle n+1 (red) line scans for the **left middle** position (a-1 and a-2) and **left corner** (b-1 and b- 2) of 60 Ah medium-Ni/graphite pouch cell, and BOD cycle 2 (purple) and BOD cycle 3 (red) for 250 mAh NMC811/graphite pouch cell (c-1 and c-2) in y-direction (top side) and x-direction (bottom side).

Figures 5.5, 5.6, and 5.7 show the full swelling profiles as a function of voltage for the left middle position, the left corner position, and the 250 mAh cell, respectively (see Figs. A.4-6 for swelling as a function of state of charge (SOC)). These graphs demonstrate that the cells show significant thickness change during cycling but return to the exact same thickness in all positions.

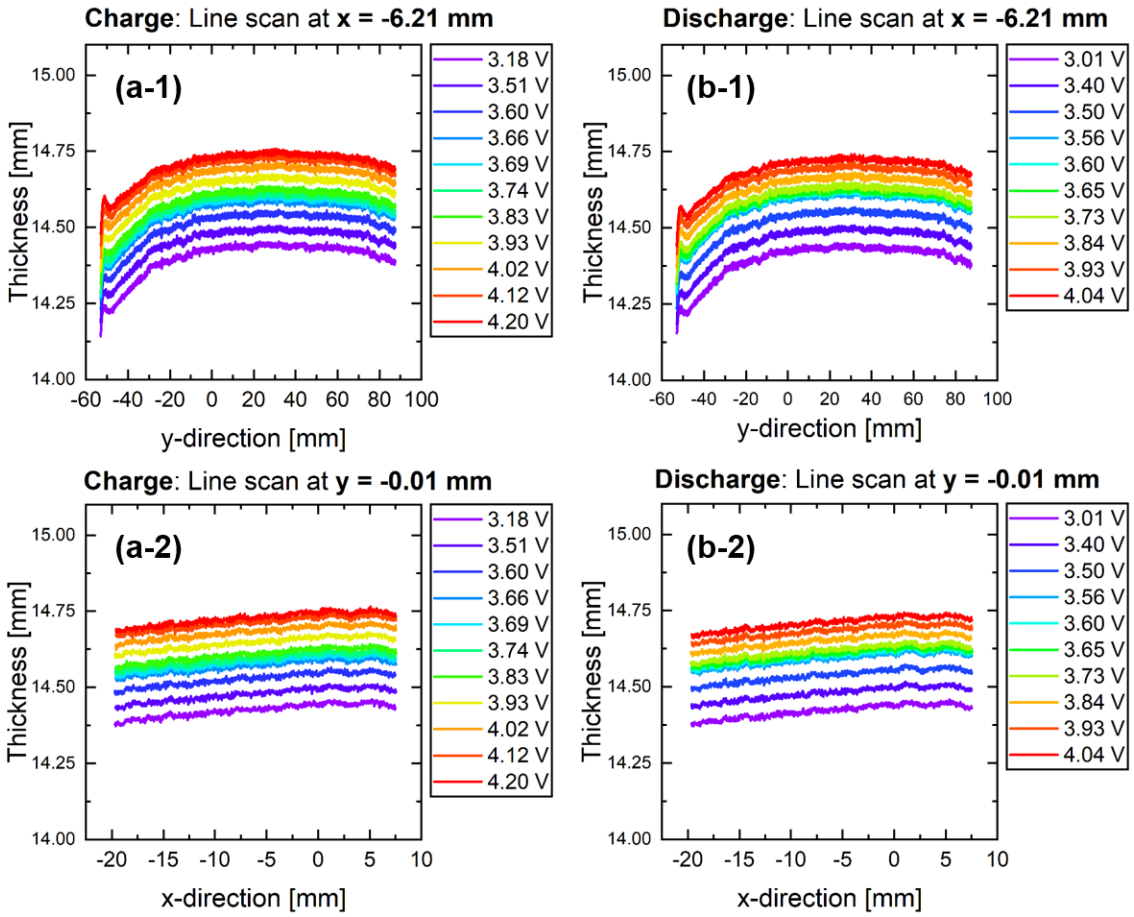

Figure 5.5: Operando line scans for **left middle position** of 60 Ah medium-Ni/graphite pouch cell during the C/10 charge step in y-direction (a-1) and x-direction (a-2) as well as line scans during the C/10 discharge step in y-direction (b-1) and x-direction (b-2). Data is reported with respect to **cell voltage.**

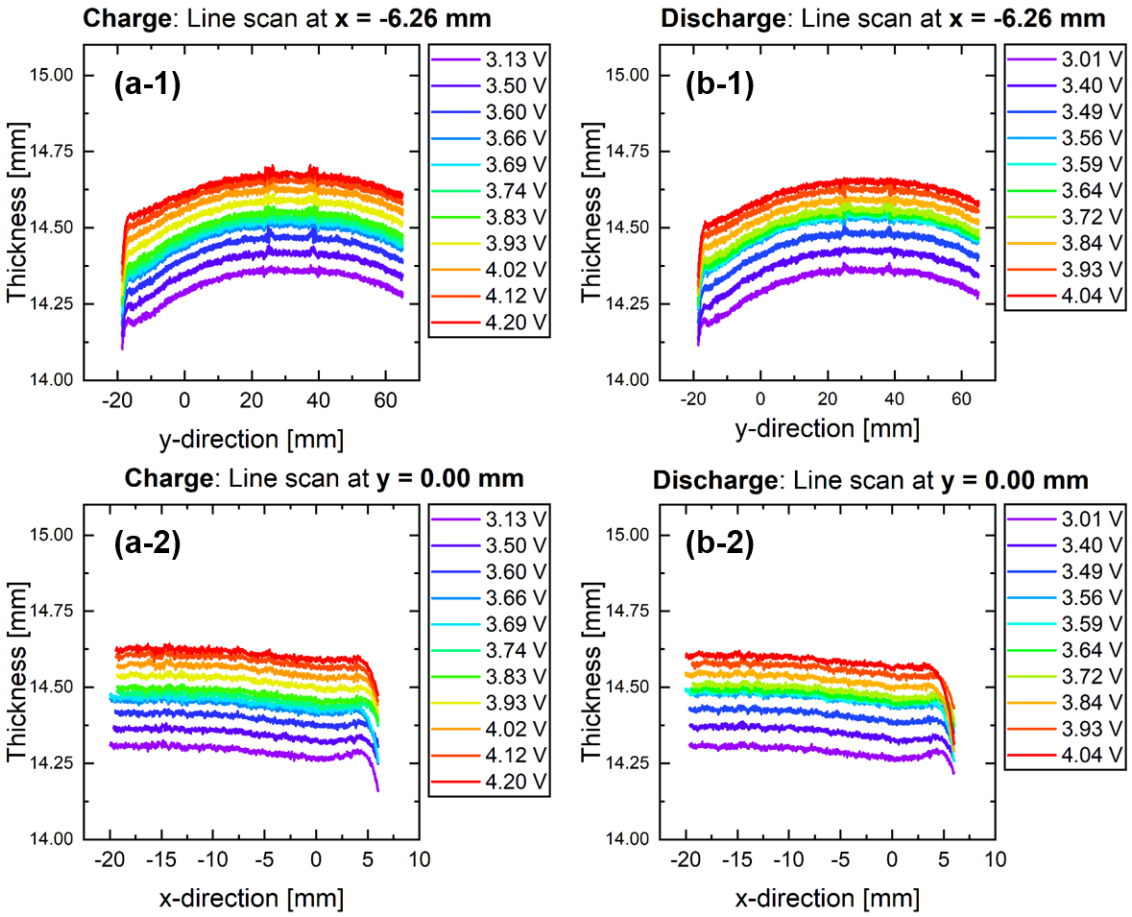

Figure 5.6: Operando line scans for **left corner** of 60 Ah medium-Ni/graphite pouch cell during the C/10 charge step in y-direction (a-1) and x-direction (a-2) as well as line scans during the C/10 discharge step in y-direction (b-1) and x-direction (b-2). Data is reported with respect to **cell voltage.**

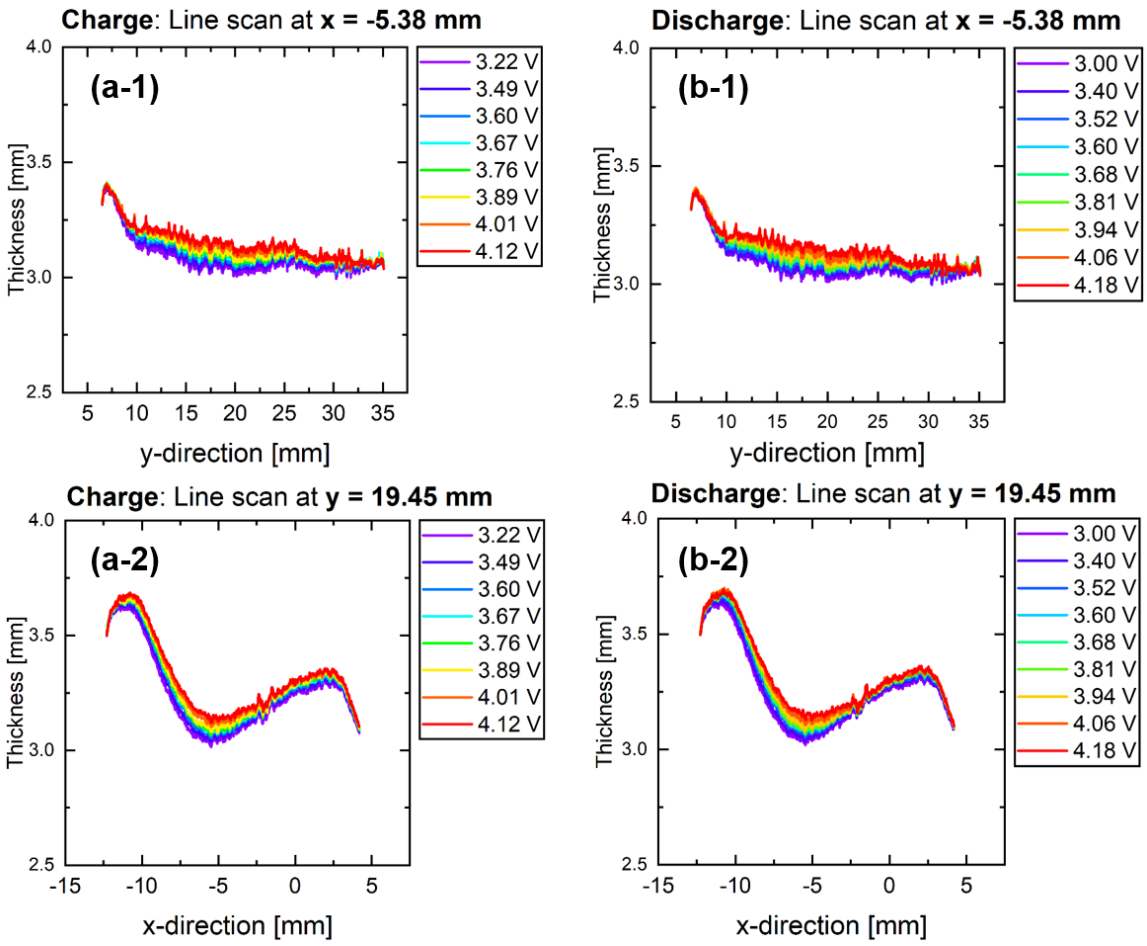

Figure 5.7: Operando line scans for **250 mAh** NMC811/graphite pouch cell during the C/10 charge step in y-direction (a-1) and x-direction (a-2) as well as line scans during the C/10 discharge step in y-direction (b-1) and x-direction (b-2). Data is reported with respect to **cell voltage.**

The data in this thesis shows that high-resolution thickness mapping can be used for quantifying cell reversibility. High quality cells with mature interfaces will not show any irreversible thickness change during cycling and thus retain their capacity very well, since no lithium is taken out of the inventory to generate reaction products that would otherwise cause irreversible swelling. High-resolution thickness mapping is a straightforward technique that provides more accurate information on cell swelling, while electrochemical signatures like the coulombic efficiency can be influenced by shuttle type reactions and must be carefully examined.

Chapter 6: Conclusions and Future Work

6.1 Conclusions

In this work, a laser scanning technique was developed to perform contact-free thickness measurements for Li-ion cells in operando with high resolution (0.57 μm in thickness direction, 15 μm in lateral direction). The method was used to monitor changes in thickness during charge and discharge, and over the course of cell aging. Measurement and quantification methods were developed and benchmarked for accuracy against traditional thickness measurement tools. The thickness mapping by the laser scanning method was the most accurate method as the non-uniform surface of the pouch cells had to be taken into consideration.

The laser scanner technique is accurate when gas and pressure discrepancies are negligible, or when the developed compression tool is used to push generated gases out of the jelly roll and into the gas bag. In Section 4.1, the high-resolution thickness mapping was used to show that irreversible processes such as SEI growth can cause irreversible thickness change. The irreversibility decreased as the cell matured (at least in the early stages of cycling tested here), though the swelling profiles were not fully reversible; there was still an accumulation of reaction products that increased cell thickness permanently. In Section 4.2, compressed cells in long-term cycling showed larger volume expansion resulting in more capacity loss for higher silicon contents. The silicon component in the silicon-graphite composite electrode also led to an asymmetric swelling profile over one complete charge/discharge cycle. The laser scanning technique was able to correlate an increase in stack thickness with an increase in pressure for volumetrically constrained cells and a decrease in the available discharge capacity. In Chapter 5, the laser scanner was able to demonstrate how volume change will vary depending on nickel content, that lab scaled pouch cells can be useful to study swelling in large automotive cells (though further studies are required to improve confidence), and that high quality cells show fully reversible swelling profiles. Though long term cycling for the high quality cells would need to be performed to assess their reversibility after significant aging.

The laser scanning technique developed here is a high-resolution method for quantifying the swelling of Li-ion cells during charge and discharge, specifically for pouch cells (less for cylindrical or prismatic), and especially when electrodes experience large volume expansion. It can determine the reversibility of swelling in large automotive cells; thus it is an important non-electrochemical method to consider for assessing the quality of commercial cells.

6.2 Future Work

This work demonstrated a new technique to quantify Li-ion cell swelling with a high degree of accuracy. In all of the studies presented in this work, electrolyte development and optimization was not the focus, thus more studies are necessary in using the laser scanner technique to assess the performance and volume change of cells with different electrolyte formulations. As well, all of the in operando volume change studies using the laser scanner were performed post formation. It would be good to learn more on how these cells behave in operando during formation where the SEI begins to form. Also, updating the operando technique to record scans at exact upper and lower cutoff voltages would be an improvement.

More work is also needed to demonstrate the versatility of the laser scanner technique, and how it can be even more useful for understanding Li-ion cell failure mechanisms. For instance, similar operando cycling experiments can be performed at different charge rates (i.e. faster) to detect lithium plating, and the scanner can be useful to learn more about the SEI by scanning Li-ion cathodes and anodes extracted from cells at different stages of aging. The laser scanner also showed how volume change can vary depending on graphite phase transitions. The contribution of volume change by silicon and graphite can be further understood by cycling the same silicon containing cells with different upper and lower cutoff voltages. Cycling cells to various cutoff voltages will impact electrochemical performance such as available capacity and reactivity of the electrodes with the electrolyte. By performing this type of study, one can learn in more detail the reasons for capacity loss, and the side reactions caused by silicon for various silicon content.[43] The laser scanner was also useful for determining the

quality of commercial cells, though more work is required to learn about how volume change applies stress to the anode tabs of large format pouch cells, and more studies are required to improve the comparisons of lab scaled pouch cells to commercial cells.

The data analysis method described in this work used a Python Code to analyze the average thickness of Li-ion pouch cells. The technique assigned a minimum and maximum threshold for the z (thickness) values which would ultimately leave some unwanted data points as being part of the average thickness calculation. Further optimization of the Python code to eliminate the unwanted data points that are not part of the pouch cell (see Fig. 3.2) would be required to further enhance the accuracy of the average thickness calculation. As well, since all graphing in this work was performed on cells with no compression, it would be a nice addition to develop a graphing method to map cell swelling of cells while using the laser scanning compression tool.

The graphing methods presented in this work are useful for mapping the distribution of swelling in cells which is important since inhomogeneity's can increase cell degradation. Thus, this scanning technology could prove to be very useful for advising the cell manufacturing process with the objective of improving the overall consistency of developing cells with homogeneous cell distributions.

The proposed future work would expand the usefulness of the laser scanning measurement system, and if successful, the laser scanner technique can become an ever-present tool for battery scientists and engineers in both industry and academia.

Appendix

A.1 Additional Data and Information

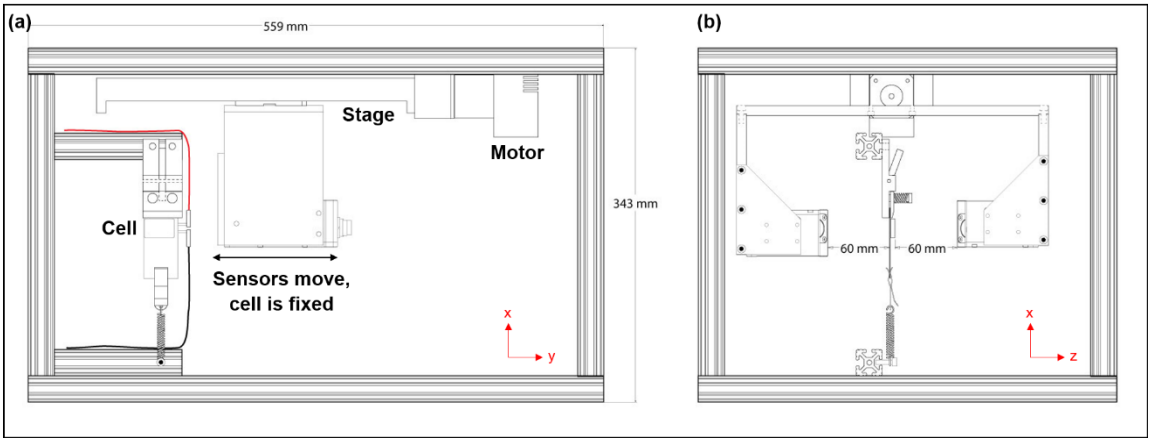

Figure A.1: Technical drawings of laser scanner setup in front view (a) and side view (b). Main parts are indicated with text.

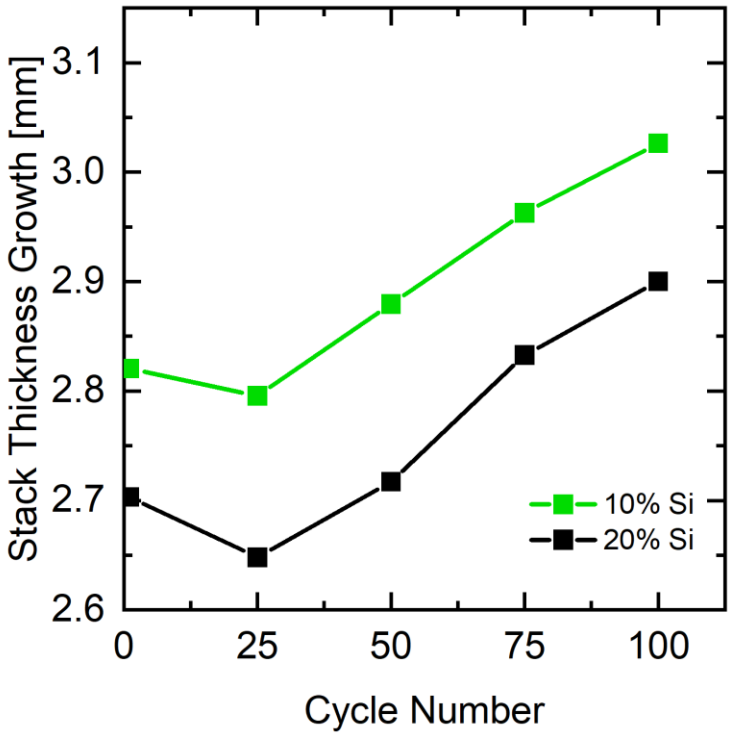

Figure A.2: Absolute stack thickness growth versus cycle number for Ni83/Si-G cells with 20% Si (black) and 10% Si (green) **with compression fixture.** The thickness measurements are taken at the BOD state, and the change in thickness is normalized to the BOD formation cycle.

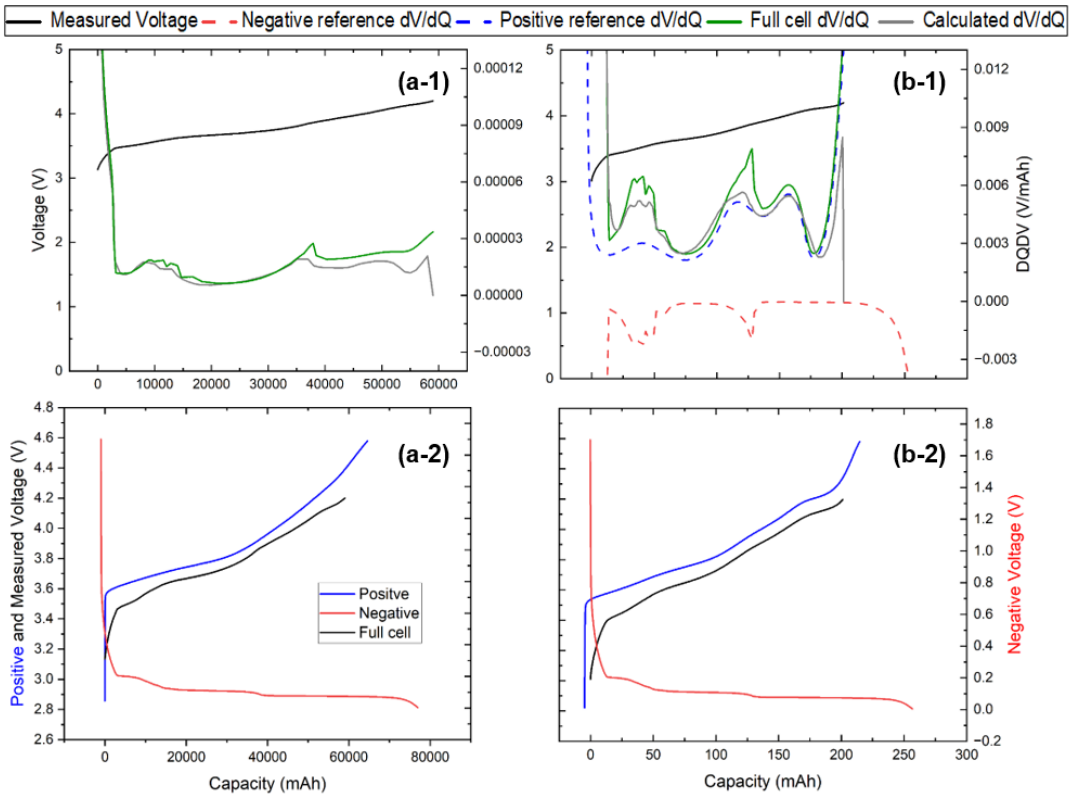

Figure A.3. dV/dQ fitting curves (top) and differential voltage vs capacity curves (bottom) for the 60 Ah medium-Ni/graphite pouch cell (a-1 and a-2), and for the 250 mAh NMC811/graphite pouch cell (b-1 and b-2).

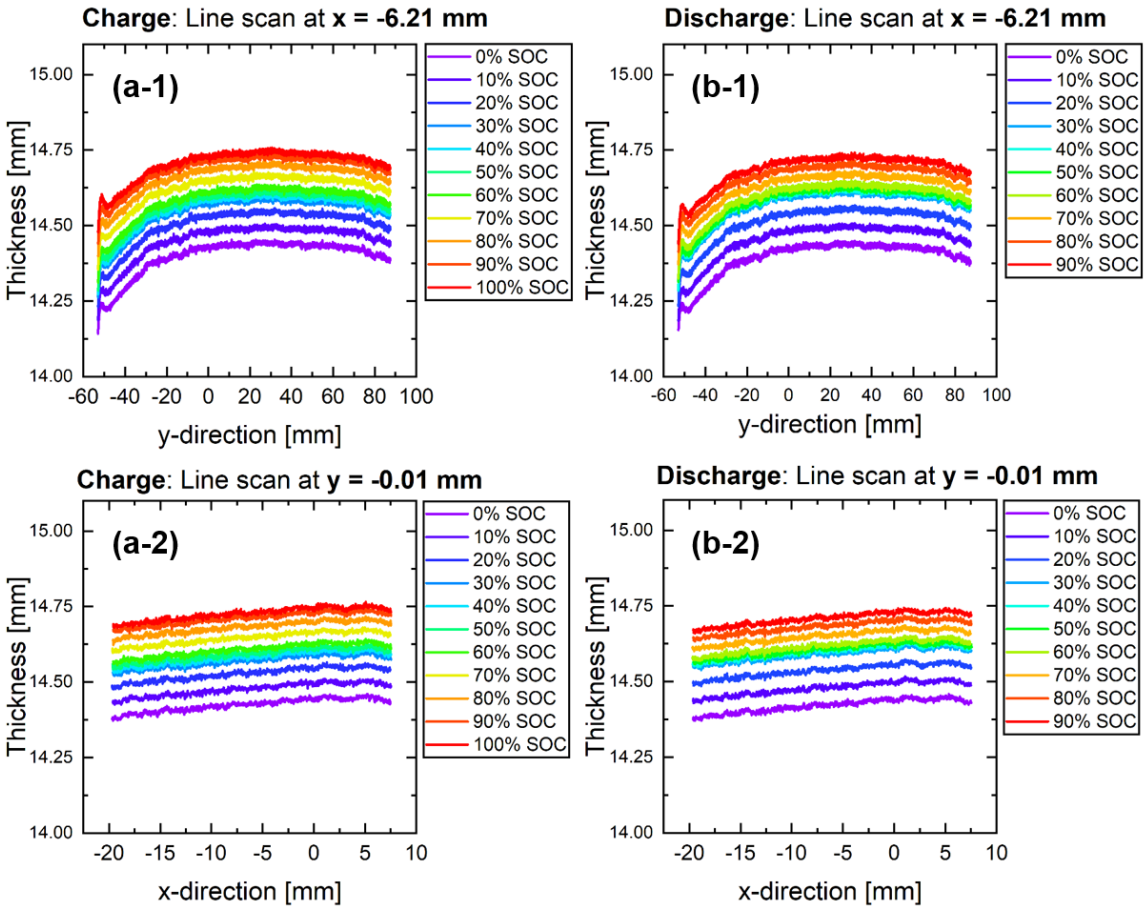

Figure A.4: Operando line scans for **left middle position** of 60 Ah medium-Ni/graphite pouch cell during the C/10 charge step in y-direction (a-1) and x-direction (a-2) as well as line scans during the C/10 discharge step in y-direction (b-1) and x-direction (b-2). Data is reported with respect to **state-of-charge.**

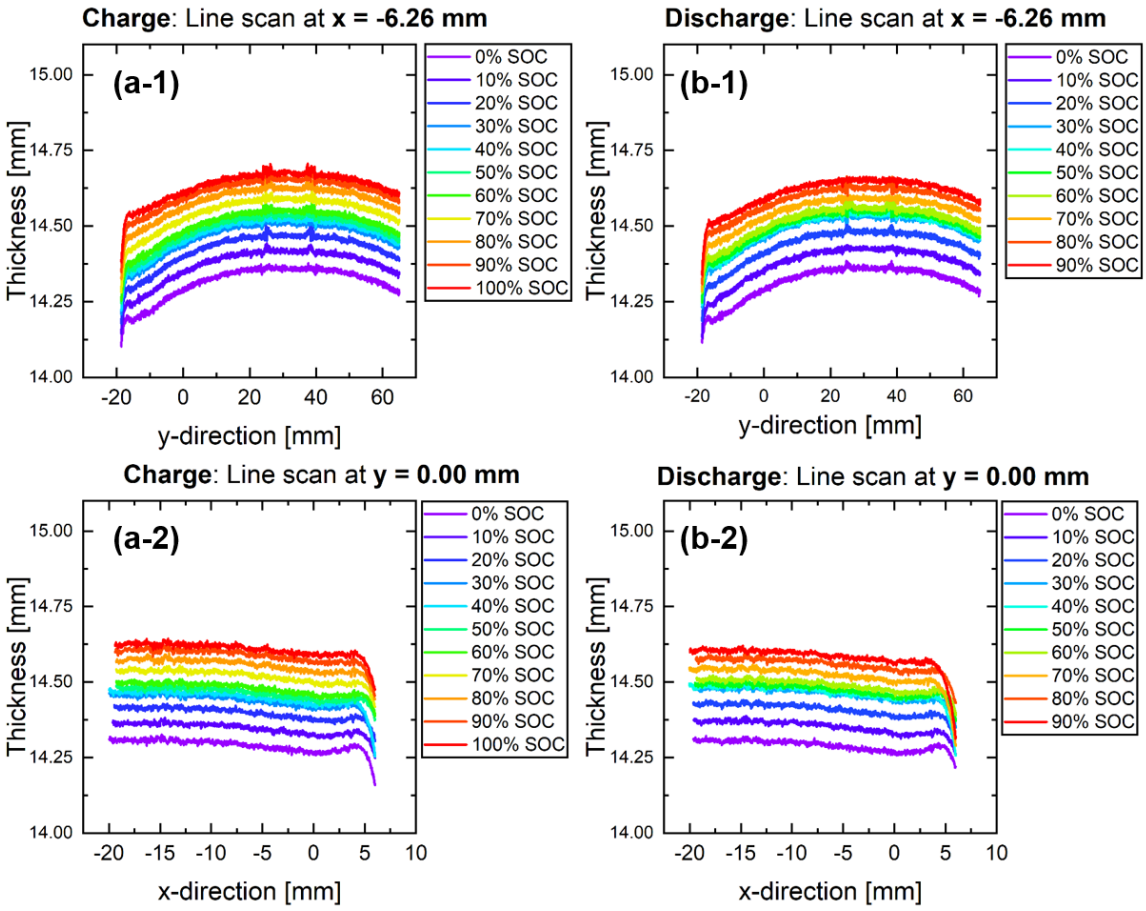

Figure A.5: Operando line scans for **left corner** of 60 Ah medium-Ni/graphite pouch cell during the C/10 charge step in y-direction (a-1) and x- direction (a-2) as well as line scans during the C/10 discharge step in y-direction (b-1) and x-direction (b-2). Data is reported with respect to **state-of-charge.**

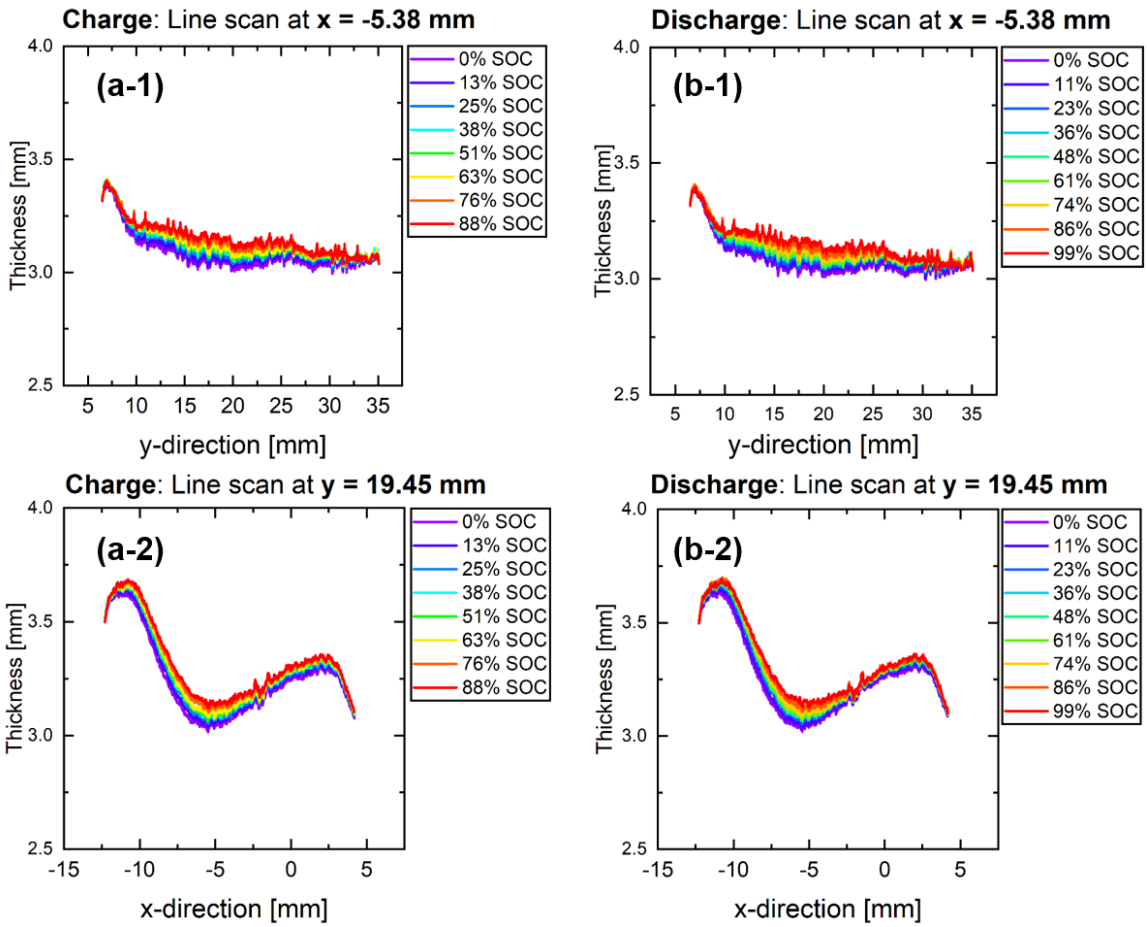

Figure A.6: Operando line scans for **250 mAh** NMC811/graphite pouch cell during the C/10 charge step in y-direction (a-1) and x-direction (a-2) as well as line scans during the C/10 discharge step in y-direction (b-1) and x-direction (b-2). Data is reported with respect to **state-of-charge.**

A.2 Python Code for Data Analysis

The following code is the Python script developed in this thesis and used for analyzing the laser scanner data.

```
# LOAD FUNCTION PACKS
import os
ROOT_DIR = os.path.abspath(os.curdir)
import pandas as pd
import numpy as np
import glob
import csv
from tkinter import filedialog
from tkinter import *
import scipy.integrate as integrate
```

```
import scipy.spatial
from scipy.spatial import Delaunay
import math
import matplotlib.pyplot as plt

#####################################################################

# Split data frame in half? 1: yes, 0: no
split = 0

# Dimensions in x (i) and y (j) direction
step = 10
delta = 3

# Stack height thresholds
z_min = 2
z_max = 4

#####################################################################

# Choose folder containing laser data
root = Tk()
root.attributes('-topmost',True)
root.after(100, root.withdraw)
print('Please choose the folder that contains the data files.')
folder_selected = filedialog.askdirectory()
# output_path = folder_selected
output_path = folder_selected + '/'
# access_rights = 0o777 # Read and write by all users
# os.makedirs(output_path, access_rights)
root.destroy()

# Create file list of Laser output files
filenames = []

filelist = glob.glob('{0}/*'.format(folder_selected))
for pathname in filelist:
    filename = os.path.basename(pathname)
    filenames.append(filename)
file_table = pd.DataFrame(filelist,columns=['pathnames'])
file_table['filenames'] = filenames

# Specifc column names for output table
Results = pd.DataFrame(columns=['filename', 'Thickness [mm]'])
Line_scan_x = pd.DataFrame()
Line_scan_y = pd.DataFrame()
```

```
for k, (filename, pathname) in enumerate(zip(file_table.filenames, file_table.pathnames)):
    print(filename)
    Results.at[k, 'filename'] = filename
    with open(pathname, 'r') as f:
        # Need to read until "Y/X" otherwise error with column designation
        df = pd.read_csv(f, skiprows=32)
        Header = pd.DataFrame(df.columns.values).transpose().loc[0:0]
        df.columns = Header.columns
        df = pd.concat([Header, df]).reset_index(drop = True)

        # Extract top scan
        Top_scan = df.loc[1:]
        Info_top = Top_scan[0]
        m=0
        while m < len(Info_top):
            if Info_top.iloc[m] == 'End':
                last_index = m
                break
            m = m+1

        Top_scan = Top_scan.loc[:last_index]
        Top_scan.index = np.arange(0, len(Top_scan))
        Info_top = Top_scan[0]
        Firstrow_top = df.loc[0:0]
        Top_scan = Top_scan.drop(columns=[0])
        Top_scan = Top_scan.astype(float)

        # Calculate gap between top and bottom scan
        gap = 6

        # Extract bottom scan
        first_index = last_index + gap
        Bottom_scan = df.loc[first_index:]
        Info_bottom = Bottom_scan[0]
        m=0
        while m < len(Info_bottom):
            if Info_bottom.iloc[m] == 'End':
                last_index = first_index + m-1
                break
            m = m+1

        Bottom_scan = Bottom_scan.loc[:last_index]
        Bottom_scan.index = np.arange(0, len(Bottom_scan))
        Bottom_scan = Bottom_scan.drop(columns=[0])
        Bottom_scan = Bottom_scan.astype(float)
```

```
        # Matrix subtraction
        Difference_scan = Top_scan.subtract(Bottom_scan)

        # Cut dataframe in half
        if split == 1:
            mid_y = round(Difference_scan.shape[0]/2)
            Difference_scan = Difference_scan.iloc[mid_y:, :]

        # Make array for thickness averaging
        xyz = Difference_scan.fillna(0).to_numpy()

        # Eliminate values that are too large or too low
        OutOfBOunds = (xyz > z_max) | (xyz < z_min)
        xyz[OutOfBOunds]=0

        # Delete all zero columns
        idx = np.argwhere(np.all(xyz[..., :] == 0, axis=0))
        xyz = np.delete(xyz, idx, axis=1)

        # Delete all zero rows
        xyz = xyz[~np.all(xyz == 0, axis=1)]

        # Plot xzy array
        plt.imshow(xyz, interpolation='nearest')

        # Alternative for averaging
        xyz[xyz == 0] = np.nan
        avg_xyz = np.nanmean(xyz, dtype=np.float64)

        # Replace NaN's with zero again
        where_are_NaNs = np.isnan(xyz)
        xyz[where_are_NaNs] = 0

        # Write results into table
        Results.at[k, 'Thickness [mm]'] = avg_xyz

        # Add X and Y coordinates back to scans
    Difference_scan.insert(loc=0, column=0, value=Info_top)
    Difference_scan = pd.concat([Firstrow_top,
Difference_scan]).reset_index(drop = True)
    Top_scan.insert(loc=0, column=0, value=Info_top)
    Top_scan = pd.concat([Firstrow_top, Top_scan]).reset_index(drop = True)
    Bottom_scan.insert(loc=0, column=0, value=Info_top)
    Bottom_scan = pd.concat([Firstrow_top, Bottom_scan]).reset_index(drop =
True)
```

```
        # Make data frame for line scan in x-direction
        Line_scan_x[0] = Difference_scan.iloc[:,0]
        mid_x = round(Difference_scan.shape[1]/2)
        insert = Difference_scan.iloc[:, mid_x]
        Line_scan_x[k+1] = insert

        # Make data frame for line scan in y-direction
        Line_scan_y[0] = Difference_scan.iloc[0,:].T
        mid_y = round(Difference_scan.shape[0]/2)
        insert = Difference_scan.iloc[mid_y, :].T
        Line_scan_y[k+1] = insert

# Write scans to csv files
Difference_scan.to_csv(output_path + filename + '_Difference_scan.csv',
index=False, header=False)
print('Difference scan for', filename, 'written')

# Output Results Table
Results.to_excel(output_path + 'Results_table.xlsx', index=False)
print('Results table written')

# Output Line Scans
Line_scan_x.to_excel(output_path + 'Line_scans_x.xlsx', index=False,
header=False)
Line_scan_y.to_excel(output_path + 'Line_scans_y.xlsx', index=False,
header=False)
print('Line scan files written')

print(len(filelist), 'files successfully analyzed')
```

A.3 Drawing for Compression Tool

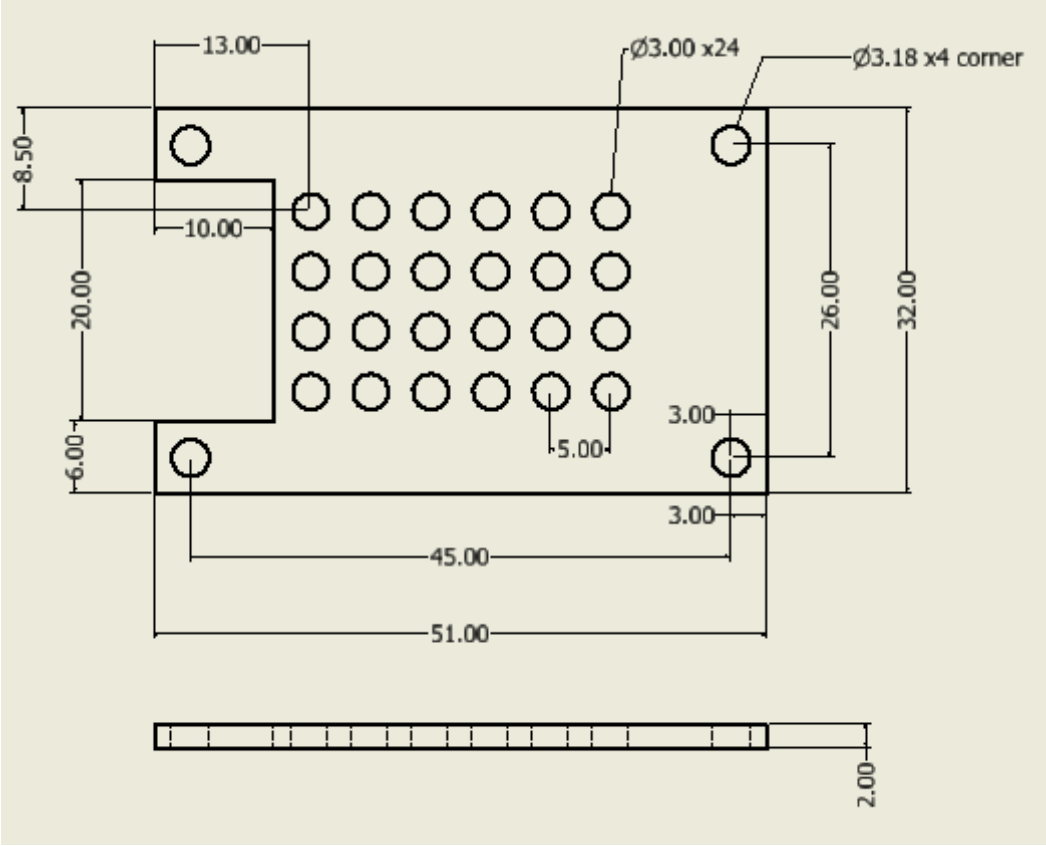

Figure A.7: A dimensioned sketch for the design of the laser scanner compression tool

A.4 Calculations

A.4.1 Estimation of Thickness Change during Charge due to Silicon Particle Expansion

Givens:

During charge; silicon particles experience a volume change of 280%, whereas graphite particles increase by 10%.

The radius of a graphite particle: $\mathbf{r_{gr}}$ **= 5.5 um**, and the radius of a silicon particle: $\mathbf{r_{si}}$ **= 1.25 um**[44]

Table A.1: Thickness details of each component that make up the jelly roll stack for **20% Si.** The number of windings for a Ni83/Si-G cell is 7.

Cell component	Single side thickness (um)	# of sides	Total thickness (um)
Anode	32.5	12	390
Copper foil	10	7	70
Cathode	64.15	12	769.8
Aluminum foil	15	7	105
Separator	15	14	210

There were parts of the cell stack neglected including a very small additional side of negative electrode and copper foil, some small amount of extra aluminum foil and separator, the tabs, and some tape.

The total cell stack thickness is the sum of the total in the table above: **t_{cell} = 1,544.8 um**

The jelly roll thickness with no pouch cell foil coverage and no electrolyte is **t_{jr} 1955.8 um**.

The difference between measured and calculated cell thickness: $t_{jr} - t_{cell} = 411$ um.

This difference is due to the neglected components of the cell stack, and the space in the middle of the jelly roll as shown in Figure A.8. This difference in space is neglected for the calculation.

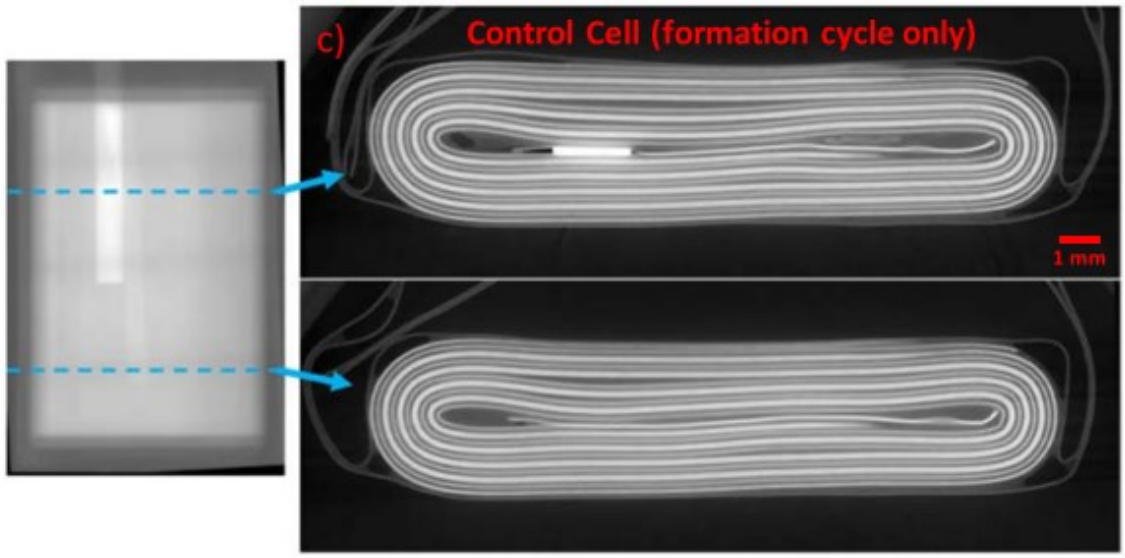

Figure A.8: A 2D CT scan cross section for a NMC622/natural graphite pouch cell that has completed only one formation cycle. This graphic was reproduced from Ref. 45.

Particle level:

The calculation for the radius change for both silicon and graphite particles are assumed to be perfect spheres.

It is assumed for the single sided layer calculation (see Fig. A.9), that the silicon and graphite particles stack on top of each other evenly within each individual layer of negative electrode (making the calculation the same for 10 or 20 Si wt%; hence the number of particles are neglected).

This is an oversimplification as you can see in Figure A.10, the graphite particles are flat, the silicon particles have an irregular shape, they do not stack evenly, and the number of particles vary.

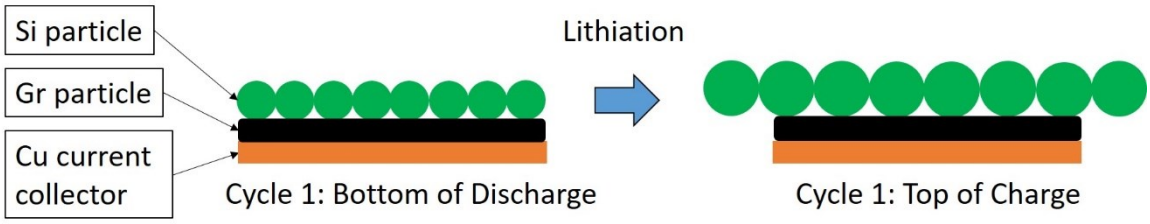

Figure A.9: Schematic of silicon and graphite particle expansion during charge. Carbon and binder are not drawn.

Volume of a graphite particle:

$$V_{gr} = \frac{4}{3}\pi r_{gr}^3 = 696.91\ \mu m^3$$

(A.1)

With a 10% increase in volume of graphite at top of charge: **V_{gr_TOC} = 766.60 um^3**

Using V_{gr_TOC} and equation A.1, the new radius of a graphite particle with 10% volume change at top of charge: **r_{gr_TOC} = 5.68 um**

The radius increase of the graphite particle is: $r_{gr\_TOC} - r_{gr}$ = **$r_{gr\_increase}$ = 0.18 um**

The increased overall thickness is the change in diameter: **$t_{gr\_increase}$ = $d_{gr\_increase}$ = 2*$r_{gr\_increase}$ = 2*0.18 µm = 0.36 um**

Using the same calculation methods, the overall thickness increase for a silicon particle is: **$t_{si\_increase}$ = 1.02 um**

<u>Layer level:</u>

Initial single particle layer thickness is the diameter of the initial graphite and silicon particles combined:

$t_{single\ layer}$ = 2*(r_{gr}+r_{si}) = 13.5 um

With single sided anode thickness = $t_{anode\ single}$ = 32.5 um

The number of layers of particles stacked on top of each other = $t_{anode\ single}/t_{single\ layer}$ = 32.5 um/13.5 um = 2.41 layers

A more specific number of particle layers can be seen in Figure A.10. The calculated number of layers has limitations, as it can be seen from the SEM image the particles are not perfect spheres and they do not stack on top of each other in a linear pattern.

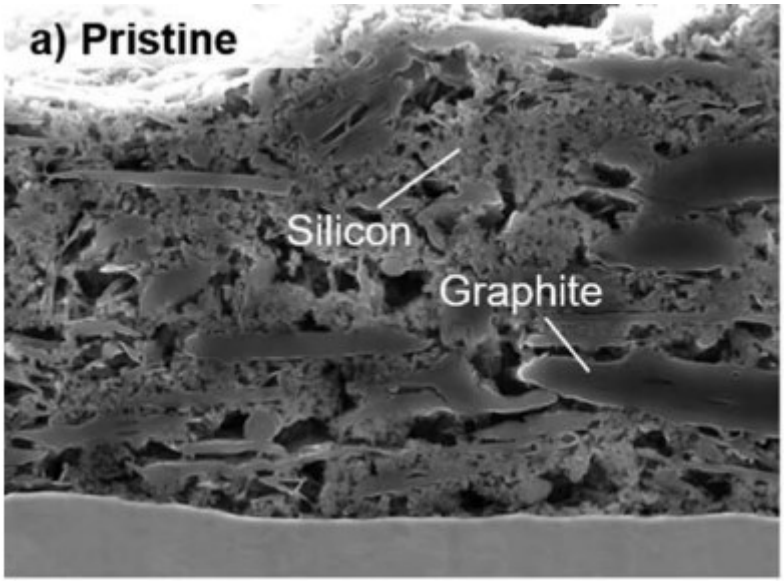

Figure A.10: A cross-sectional SEM image of a Si/G electrode in the pristine state. This graphic was reproduced from Ref 20.

The rest of the calculation will assume 3 layers of particles

The total increase in thickness for one layer of particles is:

$\mathbf{t_{single\ layer\_increase} = t_{gr\_increase} + t_{si\_increase} = 0.36\ um + 1.02\ um = 1.38\ um}$

Total particle layer thickness increase: $\mathbf{t_{layer} = t_{single\ layer\_increase} * (\#\ of\ layers) = 1.38\ um * 3 = 4.14\ um}$

Anode level:

There are 12 sides of layers within a cell stack.

Thus, the thickness increase of the overall negative electrode is: $\mathbf{t_{anode\_increase} = t_{layer} * (\#\ of\ sides) = 4.14\ um * 12 = 49.68\ um}$

Cell level:

The positive electrode can experience up to 10% change, though that change is neglected for the purposes of this calculation. It is also assumed there is no change for the copper and aluminum current collector, and separator.

The total cell stack thickness at top of charge: $t_{cell\_TOC} = t_{cell} + t_{anode\_increase}$ = **1,544.8 um + 49.68 um = 1,594.48 um**

The % increase in cell stack thickness is 3.22%

Comparison to laser scanner results:

The increase in thickness during charge for the silicon cells was lowest (2-3%) at long term cycling with compression, and highest (5-9%) in short term cycling with no compression.

This calculation is within accuracy though many assumptions were made, and there are many limitations which will be described below.

Limitations:

During cycling, the cells can experience roughening of silicon particles, inter particle resistances, reduced mechanical integrity of the electrode, impact by repeated de-lithiation on the morphology of silicon particles, and morphological damage can lead to expansion of silicon particles and porous networks. As well, SEI formation, an increase in silicon surface area which also increases SEI, volumetric changes, electrolyte decomposition products, and changes in porosity.[31]

A.4.2 Estimation of Thickness Change over Cycling

Givens:

The stack thickness growth for the Ni83/Si-G 20% cell after 100 cycles is t_{stg} = **1.0729** (7.29% increase).

The cell experienced 21% (42.5 mAh) loss in capacity.

$t_{anode\ single}$ = 32.5 um

To predict thickness increase, the main SEI component for LIBs is a component called lithium ethylene dicarbonate (LEDC), the reduction product of EC. In the formation of 1 mol of LEDC, 2 mol of lithium are consumed.[46]

The molecular weight of LEDC is **M_{LEDC} = 162 g/mol**.[47]

The assumptions made are that there are no other SEI species, which is not true when using FEC. FEC is used for this electrolyte, though FEC makes LiF and polymeric species when it is reduced at the negative electrode. When FEC is present only very little EMC is reduced.[16] Thus, the SEI no longer mainly consists of LEDC. This is neglected, and LEDC is assumed to be the only SEI component for this calculation.

The density of lithium carbonate is 2.11 g/ml.[48] Thus, the density of LEDC is assumed to be **ρ_{LEDC} = 2.11 g/ml** since it is a carbon based species which limits the accuracy of the calculation.

Faradays constant = F = 96,485,336.5 mA*s/mol = 26,801.5 mAh/mol

Volume of LEDC:

Moles of Li is the loss of lithium in mAh divided by F: **n_{Li}** = 42.5 mAh/26,801.5 mAh/mol = **1.59 x 10^-3 mol**

This produces **n_{LEDC} = 7.93 x 10^-4 mol** (1 mol Li = 0.5 mol LEDC).

The mass of LEDC is **m_{LEDC}** = M_{LEDC}*n_{LEDC} = 162 g/mol * 7.93 x 10^{-4} mol = **0.1285 g** (of LEDC)

The volume of LEDC based on capacity loss is **V_{LEDC}** = m_{LEDC} ÷ ρ_{LEDC} = 0.1285 g ÷ 2.11 g/ml **= 0.061 ml** (of LEDC)

Volume of the Negative Electrode and Pore Space:

The volume change of the positive electrode, the copper and aluminum foil, if any, are neglected for the purpose of this calculation since most of the volume change would occur in the negative electrode or at the negative electrode/separator

interface. I assume that the irreversible volume change is due to accumulation of SEI species, which starts in the pores of the negative electrode, and on the surface of the negative electrode and eventually extends into the separator pores.

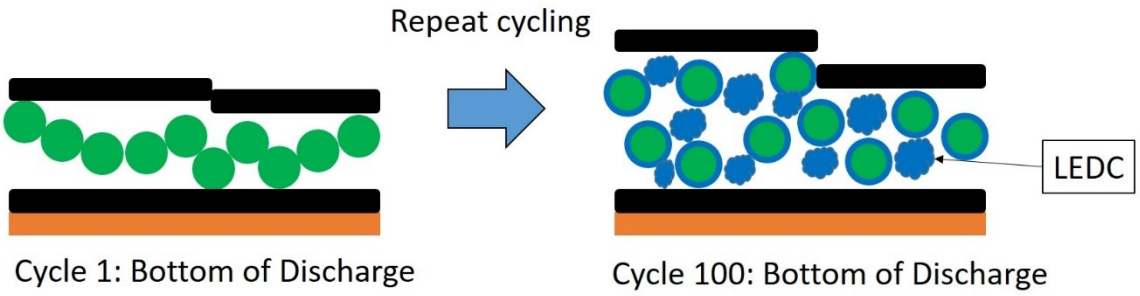

Figure A.11: Silicon and graphite particles in (left) an uncycled state and in (right) an aged silicon-graphite electrode. SEI grows over cycling causing electrode expansion. Carbon and binder are not drawn. Permanent volume change of silicon nanoparticles over long term cycling is neglected.

$\mathbf{t_{anode}} = t_{anode\ single} * 12 = 0.00325\ cm * 12 =$ **0.039 cm**

$\mathbf{V_{anode}}$ = Active area * (t_{anode}) = 65.2 cm^2 * (0.039 cm) = 2.543 cm^3 = **2.543 ml**

Assuming a porosity of 25%, based on the initial anode porosities for silicon-graphite composite anodes,[49] the volume of the pore space is:

$\mathbf{V_{pore}}$ = 0.25 * 2.543 ml = **0.636 ml**

Expected Volume Change:

The predicted cell stack increase is the % change in stack thickness growth multiplied by the original cell thickness.

For the purpose of this calculation, it is assumed the negative electrode expands by the same amount as the overall stack thickness due to the assumption the negative electrode growth contributes to most of the expansion.

$\mathbf{t_{anode\_100}} = t_{anode} * t_{stg} = 0.039cm * 1.0729 =$ **0.0418 cm**

The volume of the negative electrode at 100 cycles is $\mathbf{V_{anode\_100}}$ = Active area * (t_{anode_100}) = 65.2 cm^2 * (0.0418 cm) = 2.725 cm^3 = **2.725 ml**

Comparison:

The pore space at 100 cycles is assumed to be the same as in cycle 1.

The increase in volume over cycling is $\mathbf{V_{increase}}$ = V_{anode_100} – V_{anode} = 2.725 ml – 2.543 ml = **0.182 ml**

The volume of LEDC based the stack thickness growth measured by the laser scanner is V_{LEDC_stg} = $V_{increase}$ + V_{pore} = 0.182 ml + 0.636 ml = **0.818 ml**

Capacity loss versus stack thickness growth calculation for volume of LEDC is V_{LEDC_diff} = V_{LEDC} - V_{LEDC_stg} = 0.061 ml – 0.818 ml = -0.757 ml

Order of magnitude difference = 13.4

Limitations:

The limitations are similar to the limitations described for the calculation describing the volume change during charge.

A.4.3 Silicon-Graphite Capacity Calculation

Givens:

For this calculation, the theoretical specific capacity of graphite will be used, though due to high irreversible losses during cycling, a typical reversible capacity for silicon will be used.[29]

Specific Capacity of Silicon is $\mathbf{C_{si}}$ **= 2,319 mAh/g**

Specific Capacity of Graphite is $\mathbf{C_{gr}}$ **= 372 mAh/g**

10% Si Negative Electrode Active Mass is $\mathbf{m_{anode\_10}}$ **= 0.4951 g**

20% Si Negative Electrode Active Mass is $\mathbf{m_{anode\_20}}$ **= 0.3423 g**

Exact weight % of 10% Si cell: 9.53% Si and 85.73% graphite (carbon and binder equal 4.74%)

Exact weight % of 20% Si cell: 19.05% Si and 76.20% graphite (carbon and binder equal 4.75%)

Positive electrode capacity for both cells is $Q_{cathode}$ = 220 mAh

With an N/P ratio of 1.1, the given negative electrode capacity for both cells is **Q_{anode} = 242 mAh.**

Weight %:

Mass = m = weight % * Negative Electrode Active Mass

m_{si_10} = 0.0953 * 0.4951 = **0.0472 g** and **m_{gr_90}** = 0.8573 * 0.4951 = **0.4244 g**

m_{si_20} = 0.1905 * 0.3423 = **0.0652 g** and **m_{gr_80}** = 0.7620 * 0.3423 = **0.2608 g**

Capacity:

Capacity = Q = Specific Capacity * Mass

Q_{si_10} = 2,319 mAh/g * 0.0472 g = 109.46 mAh

Q_{gr_90} = 372 mAh/g * 0.4244 g = 157.88 mAh

Q_{anode_10} = 267.34 mAh (close to the rated 242 mAh)

% of 10% Si delivering capacity = (Q_{si_10}/Q_{anode_10}) * 100 = 40.94 %

Q_{si_20} = 2,319 mAh/g * 0.0652 g = 151.20 mAh

Q_{gr_80} = 372 mAh/g * 0.2608 g = 97.02 mAh

Q_{anode_20} = 248.22 mAh (very close to the rated 242 mAh)

% of 20% Si delivering capacity = (Q_{si_20}/Q_{anode_20}) * 100 = 60.91 %

Capacity comparison:

10% Si cell: Graphite delivers 59.06% for an extra of 48.42 mAh

20% Si cell: Graphite delivers 39.09% for a total of 54.18 mAh less than silicon

10% Si cell has 19.97% = **20% more capacity** or **102.6 mAh more capacity from graphite** relative to the 20% Si cell.

A.4.4 Compression Tool Spring Calculation

Givens:

The desired pressure for the compression tool to apply on the cell surface is 2 atm based on standard lab practice.

Pressure = P = 2 atm = 20.265 N/cm^2

Area of cell surface = A = length * width = 2.9 cm * 1.7 cm = 4.93 cm^2

Spring rate = K = 43.5 lbs/in

Compressed length at maximum load = 0.23 inches

Spring Tightening for 2 atm Pressure:

F = Force = Pressure * Area = 20.265 N/cm^2 * 4.93 cm^2 = **99.91 N**

With 4 springs applying force to the cell surface, the force of a single spring is:

$\mathbf{F_{spring}}$ = F/4 = 99.91 N/4 = 24.98 N * (0.224809 lbs/1 N) = **5.62 lbs**

To determine the desired displacement (x) of the springs:

$\mathbf{F_{spring}}$ = K*x

Thus, **x** = 5.62 lbs ÷ 43.5 lbs/in = **0.1292 inches** (which is less than the compressed length at maximum load)

Max Change in Thickness Impact on Pressure:

The maximum change in thickness calculated from BOD formation cycle to cycle 100 TOC for the Ni83/Si-G cells for both 10 and 20 wt% Si are as follows:

Maximum 10% Si change = 0.29 mm

Maximum 20% Si change = $x_{20\_increase}$ = 0.30 mm = 0.012 inches (the maximum thickness change experienced during cycling)

The increase in pressure on the cell surface is calculated as follows:

$\mathbf{F_{spring\_increase}}$ = K*x = 43.5 lbs/in * 0.012 inches = 0.522 lbs = **2.322 N**

$\mathbf{F_{increase}}$ = $F_{spring\_increase}$ *4 = **9.288 N**

Assuming the area of cell remains the same.

$\mathbf{P_{increase}}$ = $F_{increase}$/A = 9.288 N/4.93 cm2 = 1.884 N/cm2 ÷ (10.1325 N/cm^2/1 atm) = **0.186 atm**

Maximum pressure = P + $P_{increase}$ = 2 atm + 0.186 atm = **2.186 atm.**

This increase in pressure is within reason of a regular cycled cell.

Impact on Spring Integrity:

The maximum compression of the spring is $\mathbf{x_{max}}$ = x + $x_{20\_increase}$ = 0.1292 in + 0.012 in = **0.1412 in**

This is below the max compressed spring length.

Thus, the increased thickness experienced during cycling would not impact the springs as the maximum displacement does not exceed the permanent deformation point.

References

1. Alvaro Masias, James Marcicki, and William A. Paxton, ACS Energy Letters, 6, 621-630 (2021).

2. M. N. Obrovac, and V. L. Chevrier, American Chemical Society, 114, 11444-11502 (2014).

3. Toby Bond, Roby Gauthier, Sergey Gasilov, and J. R. Dahn, J. Electrochem, Soc., 169, 080351 (2022).

4. Philip Daubinger, Fabian Ebert, Sarah Hartmann, and Guinevere A. Giffin, Journal of Power Sources, 488, 229457 (2021).

5. A. J. Louli, Jing Li, S. Trussler, Christopher R. Fell, and J. R. Dahn, J. Electrochm. Soc., 164(12), A2689-A2696 (2017).

6. Emanuele Michelini, Patrick Hoschele, Simon Franz Heindl, Simon Erker, and Christian Ellersdorfer, MDPI, 9, 218 (2023).

7. Georg Fuchs, Lisa Willenberg, Florian Ringbeck, and Dirk Uwe Sauer, MDPI, 11, 6738 (2019).

8. B. Rieger, S. F. Schuster, S. V. Erhard, P. J. Osswald, A. Rheinfeld, C. Willmann, and A. Jossen, Journal of Energy Storage, 8, 1-5 (2016

9. Johannes Sturm, F. B. Spingler, B. Rieger, A. Rheinfeld, and Andreas Jossen, J. Electrochem. Soc., 164(7), A1342-A1351 (2017).

10. Yan Zhao, Franz B. Spingler, Yatish Patel, Gregory J. Offer, and Andreas Jossen, J. Electrochem. Soc., 166(2), A27-A34 (2019).

11. Xiaoqing Zhu, Zhenpo Wang, Cong Wang, and Lvwei Huang, J. Electrochem. Soc., 165 (16), A3613-A3629 (2018).

12. Zhengming Zhang, and Premanand Ramadass, Lithium-Ion Battery Systems and Technology, in: Robert A. Meyers (eds) Encyclopedia of Sustainability Science and Technology, (2012). https://doi.org/10.1007/978-1-4419-0851-3_663

13. Metrohm USA Inc.. (2022, April 12). Advancements in Li-Ion Battery Research. AZoM. Retrieved on August 28, 2023 from https://www.azom.com/article.aspx?ArticleID=19013

14. John B. Goodenough, and Kyu-Sung Park, Journal of the American Chemical Society, 135, 1167-1176 (2013).

15. Penglun Zheng, Jichang Sun, Huaiyn Liu, Rui Wang, Chuanbang Liu, Yang Zhao, Junwei Li, Yun Zheng, and Xianhong Rui, Chemistry Europe, 6 (1), 00481 (2022).

16. R. Petibon, V. L. Chevrier, C. P. Aiken, d. s. Hall, S. R. Hyatt, R. Shunmugasundaram, and J. R. Dahn, J. Electrochem. Soc., 163 (7), A1146-A1156 (2016).

17. Wentao Song, Jessie Harlow, Eric Logan, Helena Hebecker, Matthew Coon, Laurent Molino, Michel Johnson, Jeff Dahn, and Michael Metzger, J. Electrochem. Soc., 168, 090503 (2021). Bingxin Shen, Jiamin Zeng, Ning Fu, Xiadong Wang, Zhenglong Yang, Journal of Energy Storage, 55, 105767 (2022).

18. E. Peled, and S. Menkin, J. Electrochem. Soc., 164 (7), A1703-A1719 (2017).

19. Hoon-Hee Ryu, Been Namkoong, Jae-Hyuang Kim, Ilias Belharouak, Chong S. Yoon, and Yang-Kook Sun, ACS Energy Letters, 6, 2726-2734 (2021).

20. Morten Wetjen, Markus Trunk, Lukas Werner, Roman Gernhauser, Bastian Markisch, Zsolt Revay, Ralph Gilles, and Hubert A. Gasteiger, J. Electrochem. Soc., 165 (10), A2340-A2348 (2018).

21. Jake Enteistle, Anthony Rennie, and Siddarth Patwardhan, Journal of Materials Chemistry A, 6, 18344-18356 (2018).

22. Niall Kirkaldy, Mohammad Amin Samieian, Gregory J. Offer, Monica Marinescu, and Yatish Patel, Applied Energy Materials, 5, 13367-13376 (2022).

23. N. E. Galushkin, N. N. Yazvinskaya, and D. N. Galushkin, J. Electrochem. Soc., 166 (6), A897-A908 (2019).

24. Z. Mao, M. Farkhondeh, M. Pritzker, M. Fowler, and Z. Chen, J. Electrochem. Soc., 164 (14), A3469-A3484 (2017).

25. C. P. Aiken, J. Xia, David Yaohui Wang, D. A. Stevens, S. Trussler, and J. R. Dahn, J. Electrochem. Soc., 161(10), A1548 (2014).

26. Vivian Murray, David S. Hall, and J. R. Dahn, J. Electrochem. Soc., 166 (2), A329-A333 (2019).

27. T. M. Bond, J. C. Burns, D. A. Stevens, H. M. Dahn, and J. R. Dahn, J. Electrochem. Soc., 160 (3), A521-A527 (2013).

28. Hannah M. Dahn, A. J. Smith, J. C. Burns, D. A. Stevens, and J. R. Dahn, J. Electrochem. Soc., 159 (9), A1405-A1409 (2012).

29. Bingxin Shen, Jiamin Zeng, Ning Fu, Xiadong Wang, Zhenglong Yang, Journal of Energy Storage, 55, 105767 (2022).

30. A. J. Louli, L. D. Ellis, and J. R. Dahn, Joule, 3, 745-761 (2019).

31. Morten Wetjen, Sophie Solchenbach, Daniel Pritzl, Jing Hou, Vasiliki Tileli, and Hubert A. Gasteiger, J. Electrochem. Soc., 165 (7), A1503-A1514 (2018).

32. L. D. Ellis, J. P. Allen, I.G. Hill, and J. R. Dahn, J. Electrochem. Soc., 165(7), A1529-A1536 (2018).

33. J. C. Burns, Adil Kassam, N. N. Sinha, L. E. Downie, Luci Solnickova, B. M. Way, and J. R. Dahn, J. Electrochem. Soc., 160(9), A1451-A1456 (2013).

34. Bhagath Sreenarayanan, Darren H. S. Tan, Shuang Bai, Weikang Li, Wurigumula Bao, and Ying Shirley Meng, Journal of Power Sources, 531, 231327 (2022).

35. Joseph Gonalez, Ke Sun, Meng Huang, John Lambros, Shen Dillon, and Ioannis Chasiotis, Journal of Power Sources, 269, 334-343 (2014).

36. Erfan Moyassari, Thomas Roth, Simon Kucher, Chia-Chin Chang, Shang-Chieh Hou, Franz B. Spingler, and Andrea Jossen, J. Electrochem, Soc., 169, 010504 (2022).

37. Etienne Radvanyi, Willy Porcher, Eric De Vito, Alexandre Montani, Sylvain Franger, and Severine Jouanneau Si Larbi, Royal Society of Chemistry, 16, 17142 (2014).

38. Yan Jin, Bin Zhu, Zhenda Lu, Nian Liu, and Jia Zhu, Advanced Energy Materials, 7, 1700715 (2017).

39. Tao Zheng, J. N. Reimers, and J. R. Dahn, Phys. Rev. B, 51, 734 (1995).

40. Eniko S. Zsoldos, Marc M. Cormier, Mitchell Ball, Divya Rathore, and J. R. Dahn, J. Eectrochem, Soc., 170, 070502 (2023).

41. Hoon-Hee Ryu, Been Namkoong, Jae-Hyung Kim, Ilias Belharouak, Chong S. Yoon, and Yang-Kook Sun, ACS Energy Letters, 6, 2726-2734 (2021).

42. Nils Wnezler, Sebastian Rief, Sven Linden, Fabian Biebl, Samuel Rutsche, Ilona Glatt, Anja Streit, Raphael Zahn, Mathias Fingerle, and Vanessa Wood, J. Electrochem. Soc., 170 020511 (2023).

43. Erfan Moyassari, Luiza Streck, Neelima Paul, Markus Trunk, Robert Neagu, Chia-Chin Vhang, Shang-Chieh Hou, Bastian Markisch, Ralph Gilles, and Andreas Jossen, J. Electrochem. Soc., 168, 020519 (2021).

44. Chang-Hui Chen, Ferran Brosa Planella, Kieran O'Regan, Dominika Gastol, W. Dhammika Widanage, and Emma Kendrick, J. Electrochem. Soc., 167, 080534 (2020).

45. Toby Bond, Roby Gauthier, A. Eldesoky, Jessie Harlow, and J. R. Dahn, J. Electrochem. Soc., 169 (2), 020501 (2022).

46. Luning Wang, Anjali Menakath, Fudong Han, Yi Wang, Peter Y. Zavalij, Karen J. Gaskell, Oleg Borodin, Dinu Iuga, Steven P. Brown, Chunsheng, Kang Xu, and Bryan W. Eichhorn, Nature Chemistry, 11, 789-796 (2019).

47. "Lithium Ethylene Di-Carbonate," Computed by PubChem 2.1, (PubChem release 2021.05.07). Available: https://pubchem.ncbi.nlm.nih.gov/compound/Lithium-ethylene-di-carbonate. [Accessed: 2023.07.21].

48. "Lithium Carbonate," Computed by PubChem 2.1, (PubChem release 2021.05.07). Available: https://pubchem.ncbi.nlm.nih.gov/compound/Lithium-Carbonate. [Accessed: 2023.07.21].

49. Drew J. Pereira, John W. Weidner, and Taylor R. Garrick, J. Electrochem. Soc., 166 (6), A1251-A1256 (2019).